กลไกการเร่งอนุภาคที่คลื่นกระแทกซุปเปอร์ลูมินัล

นายอนันต์ อึ้งวณิชยพันธ์

หอสมุดกลาง สถาบันวิทยบริการ จุฬาลงกรณ์มหาวิทยาลัย

วิทยานิพนธ์นี้เป็นส่วนหนึ่งของการศึกษาตามหลักสูตรปริญญาวิทยาศาสตรมหาบัณฑิต
สาขาวิชาฟิสิกส์ ภาควิชาฟิสิกส์
บัณฑิตวิทยาลัย จุฬาลงกรณ์มหาวิทยาลัย
ปีการศึกษา 2542

ISBN 974-333-113-1

ลิขสิทธิ์ของบัณฑิตวิทยาลัย จุฬาลงกรณ์มหาวิทยาลัย

I19520323

PARTICLE ACCELERATION MECHANISMS AT A SUPERLUMINAL SHOCK

Mr. Anant Eungwanichayapant

A Thesis Submitted in Partial Fulfillment of the Requirements
for the Degree of Master of Science in Physics
Department of Physics
Graduate School
Chulalongkorn University
Academic Year 1999

ISBN 974–333–113-1

Thesis Tittle PARTICLE ACCELERATION MECHANISMS AT A SUPER-LUMINAL SHOCK
By Mr. Anant Eungwanichayapant
Department Physics
Thesis Advisor Associate Professor David Ruffolo, Ph.D.

Accepted by the Graduate School, Chulalongkorn University in Partial Fulfillment of the Requirement for the Degree of Master of Science.

Suchada Kiranandana .... Dean of Graduate School
(Associate Professor Suchada Kiranandana, Ph.D.)

Thesis Committee

Ahpisit Ungkitchanukit .... Chairman
(Ahpisit Ungkitchanukit, Ph.D.)

David Ruffolo .... Thesis Advisor
(Associate Professor David Ruffolo, Ph.D.)

N. Sanguansak .... Thesis Co-Advisor
(Nuanwan Sanguansak, Ph.D.)

.... Member
(Assistant Professor Pornchai Pacharin-Tanakun, Ph.D.)

Rujikorn Dhanawittayapol .... Member
(Rujikorn Dhanawittayapol, Ph.D.)

พิมพ์ต้นฉบับบทคัดย่อวิทยานิพนธ์

อนันต์ อึ้งวณิชยพันธ์ : กลไกการเร่งอนุภาคที่คลื่นกระแทกซุปเปอร์ลูมินัล
(PARTICLE ACCELERATION MECHANISMS AT A SUPERLUMINAL SHOCK)
อ. ที่ปรึกษา : รศ. ดร. เดวิด รูฟโฟโล อ. ที่ปรึกษาร่วม : ดร. นวลวรรณ สงวนศักดิ์, 72 หน้า. ISBN 974-333-113-1

เราได้พิจารณาความเป็นไปได้ของการเร่งรังสีคอสมิคที่คลื่นกระแทกซุปเปอร์ลูมินัล และได้ทดสอบในรายละเอียดสำหรับตัวอย่างของ pulsar wind termination shock เราศึกษาแบบจำลองของคลื่นกระแทกและกลไกการเร่งต่างๆ เราไม่เพียงแค่ได้ทำการปรับปรุงสมการการขนส่งที่ใช้ในกรณีนี้เท่านั้น แต่เรายังได้เขียนโปรแกรมคอมพิวเตอร์เพื่อจำลองวงโคจรของอนุภาคในแบบจำลอง pulsar wind termination shock แบบง่ายๆ โดยใช้พารามิเตอร์ต่างๆ ที่เสนอแนะโดย Gallant and Arons (1994)

จากการศึกษาวงโคจรของอนุภาคเราพบว่าอนุภาคส่วนใหญ่ไม่ได้ผ่านคลื่นกระแทกมากกว่าหนึ่งครั้ง เราคาดว่าผลจาก pitch angle scattering ควรจะมีความสำคัญ (แม้ว่าได้มีการละเลยในงานก่อนหน้านี้) ในการทำให้อนุภาคกลับมาผ่านคลื่นกระแทกอีกครั้งและได้รับพลังงานเพิ่มจากกระบวนการ shock drift acceleration จากการศึกษาเราพบว่าทั้งวิธีการศึกษาวงโคจรของอนุภาคและสมการการขนส่งไม่เพียงพอในการสร้างแบบจำลองการเร่งของอนุภาคโดยคลื่นกระแทกได้ อนุภาคเหล่านี้จะสูญเสียพลังงานภายนอกคลื่นกระแทกถ้าขนาดสนามแม่เหล็กแปรผกผันกับระยะทางจากพัลซาร์ เนื่องจากอนุภาคจะเลื่อนจากเส้นศูนย์สูตรไปสู่ขั้วซึ่งเป็นทิศทางที่อนุภาคสูญเสียพลังงาน เพราะฉะนั้นผลการจำลองของเราแสดงว่าอนุภาคพลังงานสูงที่ถูกผลิตโดยคลื่นกระแทกชนิดนี้สามารถรักษาพลังงานได้หรือไม่เมื่อเคลื่อนออกจากเนบิวลาจะขึ้นอยู่กับสมมติฐานของความสัมพันธ์ระหว่างสนามแม่เหล็กกับระยะทางจากพัลซาร์อย่างมาก

ภาควิชา ฟิสิกส์ **ลายมือชื่อนิสิต** อนันต์ อึ้งวณิชยพันธ์
สาขาวิชา ฟิสิกส์ **ลายมือชื่ออาจารย์ที่ปรึกษา** เดวิด รูฟโฟโล
ปีการศึกษา 2542 **ลายมือชื่ออาจารย์ที่ปรึกษาร่วม** นวลวรรณ สงวนศักดิ์

พิมพ์ต้นฉบับบทคัดย่อวิทยานิพนธ์ภายในกรอบสีเขียวนี้เพียงแผ่นเดียว

4072449123 : MAJOR PHYSICS
KEY WORD: SHOCK / SUPERLUMINAL SHOCK / PULSAR WIND TERMINATION SHOCK / PULSAR / THE CRAB PULSAR

ANANT EUNGWANICHAYAPANT: PARTICLE ACCELERATION MECHANISMS AT A SUPERLUMINAL SHOCK. THESIS ADVISOR: ASSOC. PROF. DAVID RUFFOLO, Ph.D. THESIS CO-ADVISOR: NUANWAN SANGUANSAK, Ph.D. 72 pp. ISBN 974-333-113-1

We consider prospects for cosmic ray acceleration at superluminal shocks and examine in detail the example of the pulsar wind termination shock. We study various models of the shock and acceleration mechanisms. Not only did we modify a transport equation for use in this case but we also wrote a computer program to simulate particle orbits in a simple pulsar wind termination shock model using the parameters suggested by Gallant and Arons (1994).

From the study of the particle orbits we found that most particles do not cross the shock more than once. We expect that pitch angle scattering effects should be important, despite their neglect in some previous work, to make a larger fraction of particles recross the shock and gain energy from shock drift acceleration. From our study we found that neither particle orbit nor transport equation methods are sufficient for modeling the acceleration of particles by the shock. However, we find that even when particles gain energy at the shock, they lose their energy outside of the shock if the magnetic field declines with the radius from the pulsar, since particles would drift from the equator to the pole which is in the direction of energy loss. Therefore, the results of our simulations show that whether high energy particles produced by this type of shock could retain that energy on their way out of the pulsar nebula depends strongly on the assumed dependence of B on r in the nebula.

ภาควิชา ฟิสิกส์ **ลายมือชื่อนิสิต**

สาขาวิชา ฟิสิกส์ **ลายมือชื่ออาจารย์ที่ปรึกษา** David Ruffolo

ACKNOWLEDGEMENTS

หอสมุดกลาง สถาบันวิทยบริการ จุฬาลงกรณ์มหาวิทยาลัย

The author wishes to express his sincere appreciation and gratitude to his advisors, Assoc. Prof. Dr. David Ruffolo and Dr. Nuanwan Sanguansak, for their valuable advice, guidance and encouragement given throughout the course of the investigation.

He would like to thank the other members of the thesis committee, Dr. Ahpisit Ungkitchanukit, Assist. Prof. Dr. Pornchai Pacharin-Tanakun and Dr. Rujikorn Dhanawittayapol for their reading and criticizing the manuscript.

He would like to thank Mr. Paisan Tooprakai and Seri Phongphanphanee for computer assistance, everyone in the Computational Astrophysics Lab for advice and Mr. Sutee Boonchui and everyone in the Forum of Theoretical Science for help.

Finally, he would like to thank the National Science and Technology Development Agency for support of this thesis.

Table of Contents

Abstract in Thai iv

Abstract in English v

Acknowledgements vi

Contents vii

List of Figures ix

List of Tables xiii

Chapter 1 Introduction 1

Chapter 2 A Specific Example: Pulsar Wind Termination Shock (PWTS) 5

- 2.1 General Structure of Pulsars 6
  - 2.1.1 Neutron Stars 6
  - 2.2.2 Pulsar Magnetosphere 13
- 2.2 The Crab Pulsar 17
- 2.3 Models of Shocks in the Crab Nebula 20

Chapter 3 Extension of Diffusive Shock Acceleration Theory to a Relativistic, Superluminal Shock 27

- 3.1 Mechanisms of Accelerating Particles 27
  - 3.1.1 First-Order Fermi Acceleration 29
- 3.2 Shocks 32

3.2.1 Subluminal Shocks 33
3.2.2 Superluminal Shocks 36
3.3 Modified Transport Equation and Rankine-Hugoniot Conditions 37
3.3.1 Modified Transport Equation 37
3.3.2 Modified Rankine-Hugoniot Conditions 40

Chapter 4 Simulation Result for a Relativistic, Quasi-Perpendicular, Superluminal Shock 45
4.1 Formulation 45
4.2 Results 49

Chapter 5 Summary and Conclusions 60

References 62
Appendix A 67
Curriculum Vitae 72

List of Figures

Figure Page

Figure 1.1 The differential energy spectra of cosmic rays measured at the top of the Earth's atmosphere for various nuclear species. 3

Figure 2.1 A 1.4 $M_\odot$ neutron star model. 7

Figure 2.2 Discovery of the first pulsar, PSR 1991+21. 9

Figure 2.3 Spin-down of the Vela radiopulsar. 10

Figure 2.4 The magnetic field of a neutron star. 11

Figure 2.5 Magnetic and electric fields about an aligned rotator. Solid lines are the dipole magnetic field lines, while the dotted lines are the electrostatic field lines, (a) for the vacuum case and (b) for the Goldreich-Julian case. 15

Figure 2.6 Magneitc field outside the light cylinder. 16

Figure 2.7 The Crab nebula (http://www.seds.org/billa/twn/orig/n1952noao.jpg). 18

Figure 2.8 WFPC2 image of the bright region of the Crab pulsar. 19

Figure 2.9 The model of the X-ray torus of Aschenbach and Brinkmann (1975). 21

Figure 2.10 A contour plot of an I-band image of the Crab nebula 22

figure 2.11 Central $100'' \times 100''$ of the Crab nebula with a resolution of $0''.5$ from the Canada-France-Hawaii Telescope. 23

Figure 2.12 Assumed equatorial wind geometry in the model of Gallant and Arons (1994). 24

Figure 2.13 The Crab nebula structure in the model of Hester et al. 25

Figure 3.1 Collision between a particle of mass m and a cloud of mass M: (a) A head-on collision, (b) a following collision. 28

Figure 3.2 Steady state of the shock in the shock rest frame. 30

Figure 3.3 Analogy for the acceleration of ions near a shock. 31

Figure 3.4 Shock in the de Hoffman-Teller frame 34

Figure 3.5 Shock in the normal incidence frame 36

Figure 4.1 A test of the program: motion of a particle in a uniform magnetic field. 48

Figure 4.2 The motion of the particle in a uniform magnetic and electric field. 48

Figure 4.3 The situation used in the simulation. 49

Figure 4.4 The result for momentum 1.92×10^{-12} kg m/s ($\gamma = 4 \times 10^6$). 50

Figure 4.5 The result for momentum 2.92×10^{-12} kg m/s ($\gamma \approx 5.82 \times 10^6$). 50

Figure 4.6 The result for momentum 3.44×10^{-12} kg m/s ($\gamma \approx 6.85 \times 10^{6}$). 51

Figure 4.7 The result for momentum 3.92×10^{-12} kg m/s ($\gamma \approx 7.81 \times 10^{6}$). 51

Figure 4.8 The result for momentum 4.10×10^{-12} kg m/s ($\gamma \approx 8.71 \times 10^{6}$). 52

Figure 4.9 The result for momentum 4.30×10^{-12} kg m/s ($\gamma \approx 8.57 \times 10^{6}$). 52

Figure 4.10 The result for momentum 4.50×10^{-12} kg m/s ($\gamma \approx 8.97 \times 10^{6}$). 53

Figure 4.11 The result for momentum 4.70×10^{-12} kg m/s ($\gamma \approx 9.37 \times 10^{6}$). 53

Figure 4.12 The result for momentum 4.80×10^{-12} kg m/s ($\gamma \approx 9.56 \times 10^{6}$). 54

Figure 4.13 The result for momentum 4.885×10^{-12} kg m/s ($\gamma \approx 9.68 \times 10^{6}$). 54

Figure 4.14 The result for momentum 4.90×10^{-12} kg m/s ($\gamma \approx 9.76 \times 10^{6}$). 55

Figure 4.15 The result for momentum 4.92×10^{-12} kg m/s ($\gamma \approx 9.80 \times 10^{6}$). 55

Figure 4.16 The result for momentum 5.00×10^{-12} kg m/s ($\gamma \approx 9.96 \times 10^{6}$). 56

Figure 4.17 The result for momentum 5.46×10^{-12} kg m/s ($\gamma \approx 10.88 \times 10^{6}$). 56

Figure 4.18 The trajectory of four cosmic rays as they pass through the nebula. In this figure only trajectory D leads to an energy gain. 59

List of Tables

Table Page

Table 2.1 Composition of neutron star material. 8

Table 2.2 Best-fit wind parameters from the model of Gallant and Arons. 22

หอสมุดกลาง สถาบันวิทยบริการ จุฬาลงกรณ์มหาวิทยาลัย

Chapter 1

Introduction

Observations of galactic cosmic rays at the top of the atmosphere show a power law distribution as in Fig. 1.1. The power law distribution can be written in mathematical form as

$$N(E)dE = KE^{\alpha}dE, \tag{1.1}$$

where the energy E is expressed in terms of the kinetic energy per nucleon and α is the power law index. To describe this distribution of cosmic rays, we need a mechanism that can accelerate particles to gain energy. The mechanism we need was found by Fermi (1949) and further developed by many investigators (e.g., Bell, 1978; Blandford and Ostriker, 1978). Today the mechanism which we use to explain the power-law spectrum is called "first-order Fermi acceleration." This mechanism usually occurs together with shock phenomena. Thus, to describe the data in Fig. 1.1 we assume that the galactic cosmic rays were accelerated at a shock. The mechanisms of shock acceleration are quite good for describing this power law spectrum. However, in our work the shock acceleration that we are interested in is different in that we hope to explain the most energetic galactic cosmic rays ($E \sim 10^{15} - 10^{18}$ eV) which are more energetic than those accelerated by supernova remnants. The maximum energy of particles from supernova remnants is about 10^{15} eV (Lagage and Cesarsky, 1983) and the particles that have an energy greater than $10^{18.5}$ eV are expected to be extragalactic (i.e., from other galaxies). Therefore, the origin of cosmic rays in the range $10^{15} - 10^{18}$ eV is still an unsolve problem. Pulsar magnetospheres are a possible candidate for the sources of the most energetic galactic cosmic rays (Hillas, 1984; Bell, 1992; Lucek and Bell, 1994) because of the high electrostatic potential in such regions.

For the shock acceleration mechanisms of less energetic galactic cosmic rays, the shock front velocity compared with the flow upstream is much less than the velocity of light. On the other hand, the shocks that we are interested in have a velocity compared with the flow upstream that is near the velocity of light. In fact, the shocks we are interested in are called superluminal shocks, as classified by the velocity of the intersection between the shock front and a given magnetic field line.

The study of the mechanisms of acceleration of particles in superluminal shocks in our work separates into two parts. The first part considers pulsar wind termination shocks as candidate shocks for high energy galactic cosmic ray acceleration as a case study. The pulsar that we choose to examine is the Crab pulsar because it is the nearest, brightest, and isolated pulsar. The other part considers a modified transport equation and Rankine-Hugoniot conditions for superluminal shocks.

In Chapter 2 we discuss our specific example for the studying superluminal shocks: pulsar wind termination shocks. In this chapter we give general knowledge about pulsars or neutron stars, and the model of the crab pulsar which is concerned with the structure of the pulsar wind termination shock.

In Chapter 3 we modify a cosmic ray transport equation and Rankine-Hugoniot conditions for use in the relativistic flow.

In Chapter 4 we simulate the trajectory of protons ejected from the Crab pulsar through the structure of the pulsar magnetic field, both inside and outside the shock.

The last chapter gives the conclusions. We draw some conclusions about

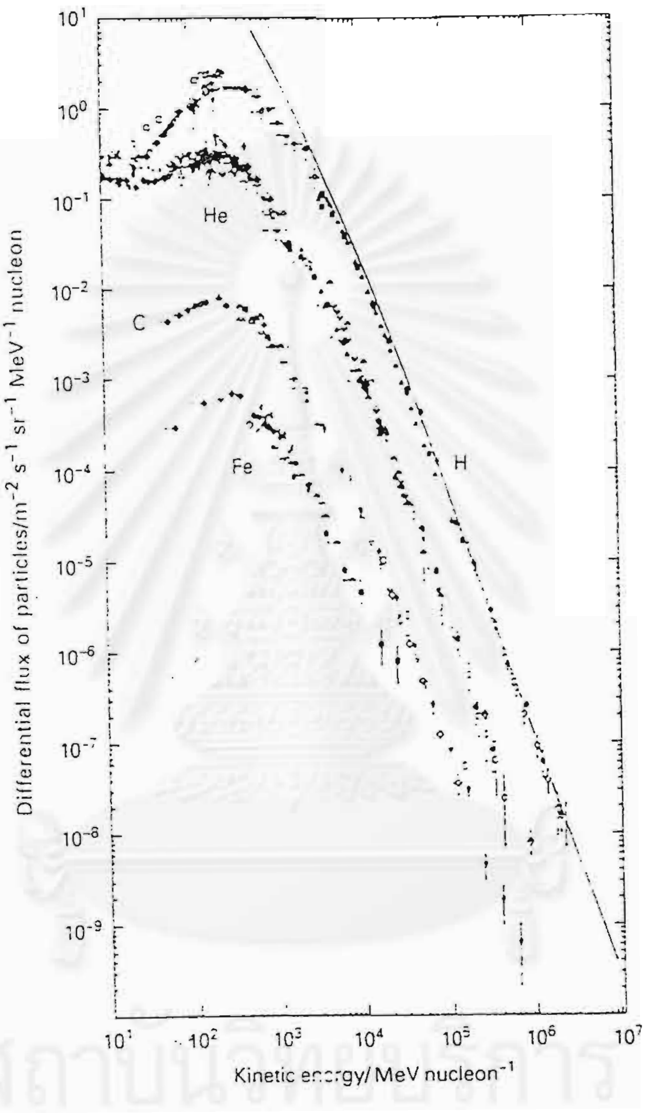

Figure 1.1: The differential energy spectra of cosmic rays measured at the top of the Earth's atmosphere for various nuclear species (Longair. 1997).

the Crab pulsar in connection with the structure of its pulsar wind termination shock and the results of the simulations.

หอสมุดกลาง สถาบันวิทยบริการ
จุฬาลงกรณ์มหาวิทยาลัย

Chapter 2

A Specific Example: Pulsar Wind Termination Shocks (PWTS)

The accidental discovery of a pulsar in 1967 (Hewish et al., 1968) was one of the most interesting events in astrophysics. The various models describing both the pulsar structure and the interactions with their surrounding nebula have been developed through 30 years after the finding. Now we know that pulsars are neutron stars which have about a 10^{12} G magnetic dipole field and rotate very fast. Radio was the first range of frequencies of electromagnetic waves that was used to study pulsars; thereafter, we use many frequency ranges to study them, including visible light and X-rays. The Crab nebula is the best-observed pulsar nebula, and we can study it as the prototype of other pulsars because it is the brightest and nearest pulsar. Not only the Crab pulsar but also the surrounding Crab nebula is interesting. The linearly polarized light from some emitting regions of the Crab nebula implies that there is synchrotron radiation in the Crab nebula, according to Shklovskii's prediction in 1953 (Shklovskii, 1953) Some data strongly suggest that there should be shocks within our Galaxy which can accelerate particles to 10^{18} eV. Pulsar wind termination shocks (PWTS) are potential candidates. A PWTS is a superluminal shock in which the flow velocity upstream is near the velocity of light. For the Crab nebula, we expect the PWTS to be located at about 0.1 R_{neb}, where R_{neb} is the radius of the nebula. Because of high-quality observations for this system, we use the Crab nebula as a specific example for the study of superluminal shocks.

2.1 General Structure of Pulsars

After the discovery of a pulsar in 1968, there have been many models to describe the phenomena of pulsars. This section will discuss some general structures of pulsars.

2.1.1 Neutron Stars

Neutron stars are superdense stars that are believed to result from supernova explosions. From the theory of stellar evolution we know that stars are in equilibrium when the contracting force due to gravitation equals the thermal pressure due to nuclear reactions, depending on what state the star is in. The nearest example of this is the Sun of our solar system. It is in an intermediate state of stellar evolution and is in equilibrium between the gravitational force and the thermal pressure that comes from burning hydrogen to helium. This state will go on for about another 5×10^9 years and then change to the red-giant phase when it burns out its hydrogen. After that, it will become a white dwarf, sustained by electron degeneracy pressure. For more massive stars, the next state is burning helium, followed by a whole sequence of states, each leading to the next state by burning the product of the current state. However, for very massive stars, when the evolution goes to the state of producing iron, the element with the highest binding energy per nucleon, there are no more elements to burn exothermically, so the dominant gravitational force will collapse the star. Electron degeneracy pressure cannot support a core mass greater than the Chandrasekhar mass, $M_{ch} \approx 1.46 M_{\odot}$. Therefore, for such a massive star, the density of the star will increase until reaching the density at which degenerate neutron pressure, due to the Pauli exclusion principle, can balance the gravitational force. The internal structure of neutron stars is also a field that many astrophysicists are interested in. We will not discuss about the structure inside neutron stars in detail. However, we will show the rough structure inside neutron stars in Table 2.1 and Fig. 2.1 (Ostlie and Carroll, 1996)

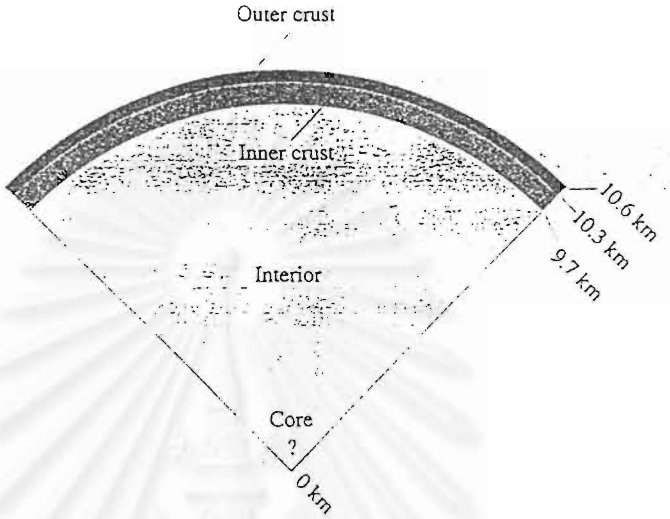

Figure 2.1: A 1.4 $M_\odot$ neutron star model (Ostlie and Carroll, 1996).

The first observed radio pulses (in 1968) have a period of 1.377 s at a frequency of 81.5 MHz (Lipunov, 1992; Fig.2.2) This indicates that magnetized neutron stars are the source because the pulses have a short and regular period.

Conservation of angular momentum provides the explanation. As the star's core contracts,

$$\begin{aligned} I_i\omega_i &= I_f\omega_f \\ M\frac{2}{5}R_i^2\omega_i &= M\frac{2}{5}R_f^2\omega_f \\ \frac{\omega_i}{\omega_f} &= \left(\frac{R_f}{R_i}\right)^2, \end{aligned} \tag{2.1}$$

where the subscripts i and f refer to initial and final states respectively. Written

Transition density ($g\ cm^{-3}$)	Composition	Degeneracy pressure
	iron nuclei, nonrelativistic free electrons	electron
$\approx 1 \times 10^6$	electrons become relativistic	
	iron nuclei, relativistic free electrons	electron
$\approx 1 \times 10^9$	neutronization	
	neutron-rich nuclei, relativistic free electrons	electron
$\approx 4 \times 10^{11}$	neutron drip	
	neutron-rich nuclei, free neutrons, relativistic free electrons	electron
$\approx 4 \times 10^{12}$	neutron degeneracy pressure dominates	
	neutron-rich nuclei, superfluid free neutrons, relativistic free electrons	neutron
$\approx 2 \times 10^{14}$	nuclei dissolve	
	superfluid free neutrons, superconducting free protons, relativistic free electrons	neutron
$\approx 4 \times 10^{14}$	pion production	
	superfluid free neutrons, superconducting free protons, relativistic free electrons, other elementary particles (pions, ...?)	neutron

Table 2.1: Composition of neutron star material (Ostlie and Carroll, 1996).

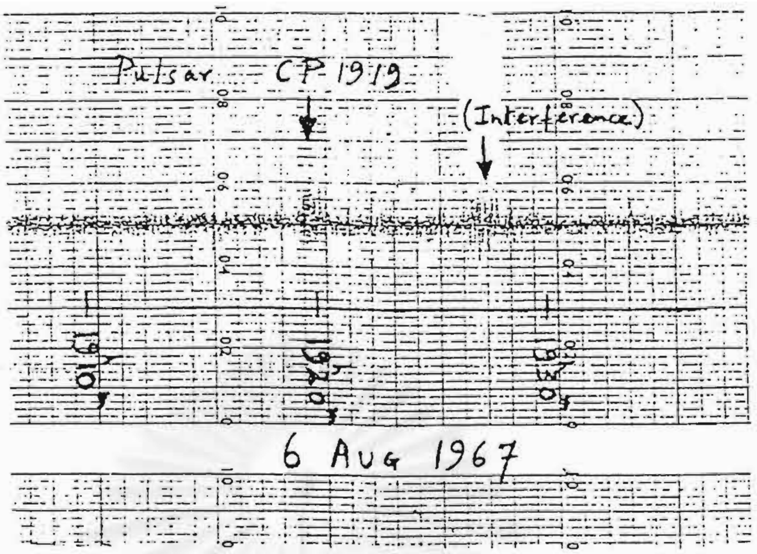

Figure 2.2: Discovery of the first pulsar, PSR 1991+21 (Ostlie and Carroll, 1996).

in terms of the rotation period, P, this is

$$P_f = P_i \left(\frac{R_f}{R_i}\right)^2 \tag{2.2}$$

Neutron stars are compact stars that evolve from supergiant stars, so the rotation period, which changes as the radius of the stas squared, is so short, on the order of a few milliseconds. For example, if our Sun were to become a neutron star which has radius about 10^4 m, its period would become about 10^{-4} s. Not only is there a uniform and short period signal received from pulsars, but the data also show a spin-down of periods of neutron stars, as shown in Fig. 2.3.

This figure shows that the periods of the pulsars are longer than in the past, indicating that there is a loss of rotational energy of the pulsars; in fact the rate of the spin-down is consistent with dipole radiation from the expected dipole magnetic field.

The other important property of neutron stars is their magnetic fields. It is strongly believed that magnetic fields near neutron stars are in dipole form as

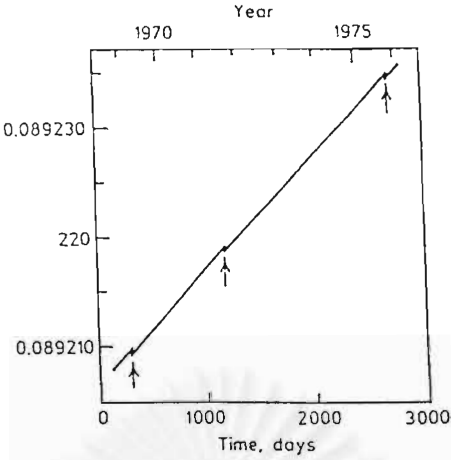

Figure 2.3: Spin-down of the Vela radiopulsar (Lipunov, 1992).

in Fig. 2.4. Then the magnetic dipole field of a neutron star, like any general magnetic dipole field, is

$$\mathrm{B} = \frac{2m\cos\theta}{R^3}\mathrm{e}_\mathrm{r} + \frac{m\sin\theta}{R^3}\mathrm{e}_\theta, \tag{2.3}$$

where e_r and e_θ are unit vectors in the directions of radius and polar angle, respectively, and m is the magnetic dipole moment,

$$m = \frac{B_0 R_0^3}{2}, \tag{2.4}$$

where B_0 and R_0 are the magnetic field strength and radius at the pole of the neutron star, respectively. The magnitude of the magnetic field of the neutron star is also huge, on the order $10^8 - 10^{12}$ G. Like the rotation speed, the tremendous magnetic field strength comes from the evolution of the star and the principle of conservation of magnetic flux. The flux of a magnetic field, Φ, through a surface S is defined as the surface integral

$$\Phi \equiv \int_S \mathrm{B} \cdot d\mathrm{A}.$$

In approximate terms, if we ignore the geometry of the magnetic field, this means that the product of the magnetic field strength and the area of the star's surface

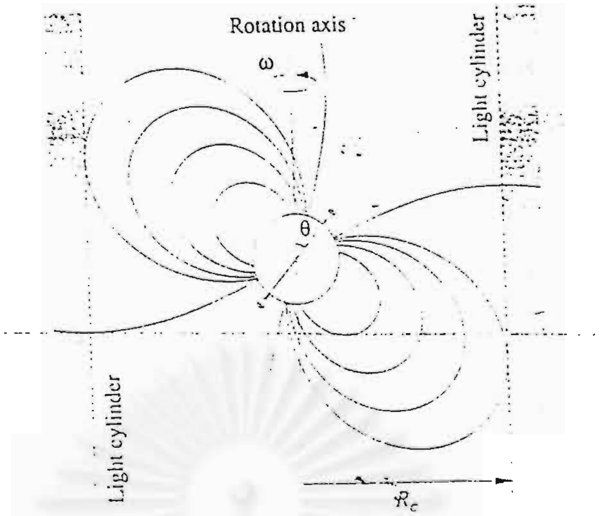

Figure 2.4: The magnetic field of a neutron star (Ostlie and Carroll, 1996).

remains constant. Thus

$$\begin{aligned} B_i 4\pi R_i^2 &= B_f 4\pi R_f^2 \\ B_f &= B_i \left(\frac{R_i}{R_f}\right)^2 \end{aligned} \tag{2.5}$$

It is not at all clear what should be considered as the value of the initial magnetic field of an iron core at the center of a presupernova star. As an extreme case, we can use the largest observed white-dwarf magnetic field of $B \approx 5 \times 10^8$ G. Then the magnetic field of the neutron star would be

$$\begin{aligned} B_{ns} &\approx B_{wd} \left(\frac{R_{wd}}{R_{ns}}\right)^2 \\ &\approx 1.3 \times 10^{14}\mathrm{G} \end{aligned}$$

where $R_{wd}/R_{ns} \approx 512$ (Ostlie and Carroll, 1996). This shows that neutron stars could be formed with extremely strong magnetic fields, although this particular estimate must be viewed as an upper limit rather than a typical value.

Two main properties, the strong magnetic dipole field and fast rotation, of neutron stars are the origin of almost everything that we observe. The first observed data received from pulsars were radio pulses. We can estimate the magnetic field strength of the pulsar from the radio pulsars which we observed. We know from Fig. 2.2, the increase in the period, that pulsars are spinning down, so if the rotation energy of the neutron stars changes mainly to magnetic dipole radiation energy, we can calculate rates of the loss of the rotation energy:

$$\begin{aligned}\frac{dE}{dt} &= \frac{d\left(\frac{1}{2}I\omega^2\right)}{dt} \\ &= 2\pi^2 I\frac{d}{dt}\left(\frac{1}{P^2}\right) \\ \dot{E} &= -\frac{4\pi^2 I}{P^3}\dot{P}, \end{aligned} \tag{2.6}$$

where I, ω and P are the moment of inertia, angular velocity and period of rotation of neutron stars, respectively. Next, we consider the power of magnetic dipole radiation (Jackson, 1975),

$$\frac{d\mathcal{P}}{d\Omega} = \frac{c}{8\pi}Re\left[r^2\mathbf{n}\cdot\mathbf{E}\times\mathbf{B}^*\right] \tag{2.7}$$

where Ω is the solid angle, **n** is the unit vector that points to the observer, B and **E** are magnetic and electric fields, and $\mathcal{P}$ is the power from the radiation.[1] For this case (Jackson, 1975)

$$\mathrm{B} = k^2(\mathrm{n}\times\mathrm{m})\times\mathrm{n}\frac{e^{ikr}}{r} + [3\mathrm{n}(\mathrm{n}\cdot\mathrm{m})-\mathrm{m}]\left(\frac{1}{r^3}-\frac{ik}{r^2}\right)e^{ikr} \tag{2.8}$$

and

$$\mathrm{E} = -k^2(\mathrm{n}\times\mathrm{m})\frac{e^{ikr}}{r}\left(1-\frac{1}{ikr}\right). \tag{2.9}$$

In Eqs. 2.8 and 2.9, **m** refers to the magnetic dipole moment whose magnitude appeared in Eq. 2.4. Then using Eqs. 2.7, 2.8 and 2.9 we will get

$$\frac{d\mathcal{P}}{d\Omega} = \frac{c}{8\pi}k^4\left|(\mathrm{n}\times\mathrm{m})\right|^2$$

---

[1] $\mathbf{B}^*$ is the complex conjugate of the magnetic field **B**; **E** and **B** are expressed as complex wave functions.

$$\begin{aligned}\mathcal{P} &= \int \frac{c}{8\pi} k^4 \left|\mathbf{m}\right|^2 \sin^2\theta d\Omega \\ \mathcal{P} &= -\frac{4\pi^4 B_0^2 R^6}{3c^3 P^4}, \end{aligned} \tag{2.10}$$

where the minus sign implies a loss of energy. Assuming that the rotation energy is transferred to magnetic dipole radiation, we equate Eqs. 2.6 and 2.10:

$$\frac{4\pi^4 B_0^2 R^6}{3c^3 P^4} = \frac{4\pi^2 I \dot{P}}{P^3}. \tag{2.11}$$

From the equality we can estimate the value of the magnetic field at the pole of a neutron star:

$$B_0 = \frac{\sqrt{3c^3 I P \dot{P}}}{\pi R^3}. \tag{2.12}$$

We will use the Crab pulsar as an example of this approximation. The Crab pulsar has a radius of about 10^6 cm (Ostlie and Carroll, 1996), a mass of about 1.4 $M_\odot$ and a period and rate of period increase of 0.0333 seconds and 421.288×10^{-15}, respectively. The magnetic field strength at the pole, by Eq. 2.12, is about 3.8×10^{12} G.

2.1.2 Pulsar Magnetosphere

The interaction between a pulsar and its surrounding nebula is also important. This interaction is the effect of the two main properties of pulsars or neutron stars, their rotation and magnetic dipole field. The PWTS is concerned with or at least based on this interaction. We will discuss this interaction only briefly because pulsar magnetospheres comprise a broad topic with many models, like neutron star structure.

The mass of a neutron star is great, $\approx 1.4 M_\odot$, but the radius is very small, $\approx 10^5$ cm, so the attractive gravitational force is huge. Does this imply that there is a vacuum outside of pulsars? No. Goldreich and Julian (1969) showed that there is an electric field, due to the rotation and magnetic field of neutron stars, leading to the conclusion that a rotating magnetic neutron star cannot be surrounded by a vacuum. Their model, which is an idealized model, with aligned spin and rotation axes, shows that there is an electric field component parallel to the magnetic field:

$$\mathbf{E}\cdot\mathbf{B} = -\left(\frac{\Omega R}{c}\right)\left(\frac{R}{r}\right)^7 B_0^2\cos^2\theta. \tag{2.13}$$

However, for a more realistic model, Mestel (1971) showed that the component of the electric field parallel to the magnetic field of a rotating neutron star with its rotation axis and magnetic dipole axis inclined by a relative angle χ was:

$$\begin{aligned}\mathbf{E}\cdot\mathbf{B} \;\simeq\; & -\left(\frac{\Omega R}{c}\right) B_0^2\cos\theta \\ & \times[\cos^2\chi\cos^2\theta + \sin^2\chi\cos^2\theta\sin^2\theta \\ & +2\sin\chi\cos\chi\cos\theta\sin\theta\cos\varphi].\end{aligned} \tag{2.14}$$

This electric field has more influence than the gravitational force, so electrons and ions on the surface will be pulled up from the surface. After the particles are pulled up, the magnetic field will be along the equipotential lines of the electric field, as in Fig. 2.5. If magnetic field lines are along equipotentials, then it immediately follows that the plasma motion, which is just the $\mathbf{E}\times\mathbf{B}/B^2$ drift velocity (neglecting any motion along field lines), corresponds to rigid corotation of the plasma with the pulsar. The plasma does not rotate as a rigid body structure; this rotation appears only in the cylindical region with a radius smaller than the light cylinder radius, R_{lc}, which was defined by Gold (Gold, 1968 cited by Michel, 1991) as

$$R_{lc} \equiv \frac{c}{\Omega}. \tag{2.15}$$

This corresponds to the radius at which the corotation speed is c; beyond this corotation is not physically possible. Beyond the light cylinder radius the magnetic field will be dragged by the plasma. Thus, the structure of the magnetic

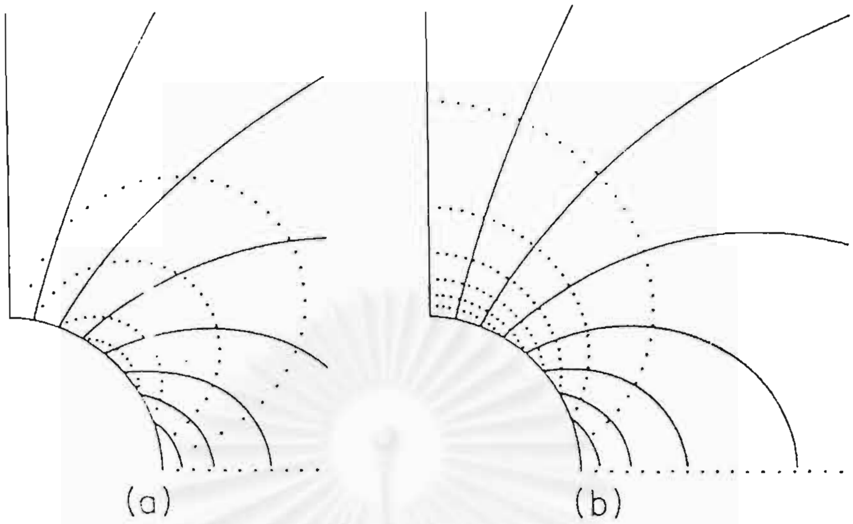

Figure 2.5: Magnetic and electric fields about an aligned rotator. Solid lines are the dipole magnetic field lines, while the dotted lines are the electrostatic field lines, (a) for the vacuum case and (b) for the Goldreich-Julian case (Michel, 1991).

field of the pulsar within the light cylinder is a poloidal field and outside light cylinder is a toroidal field as in Fig. 2.6.

For plasma in the pulsar's magnetosphere, there are not only particles at the pole of pulsar, which are pulled up by the electric field along the magnetic field, but there are also electron-positron pairs (Arons, 1979; 1983 cited in Michel, 1991). These pairs are created by the charged particles ejected from the vicinity of the pulsar's magnetic pole and are quickly accelerated to a relativistic velocity by the electric field along the curved magnetic field. The charged particles will radiate energetic photons by curvature radiation. The photons have so much energy that they can spontaneously undergo electron-positron pair production, as in this equation

$$\gamma \longrightarrow e^- + e^+, \tag{2.16}$$

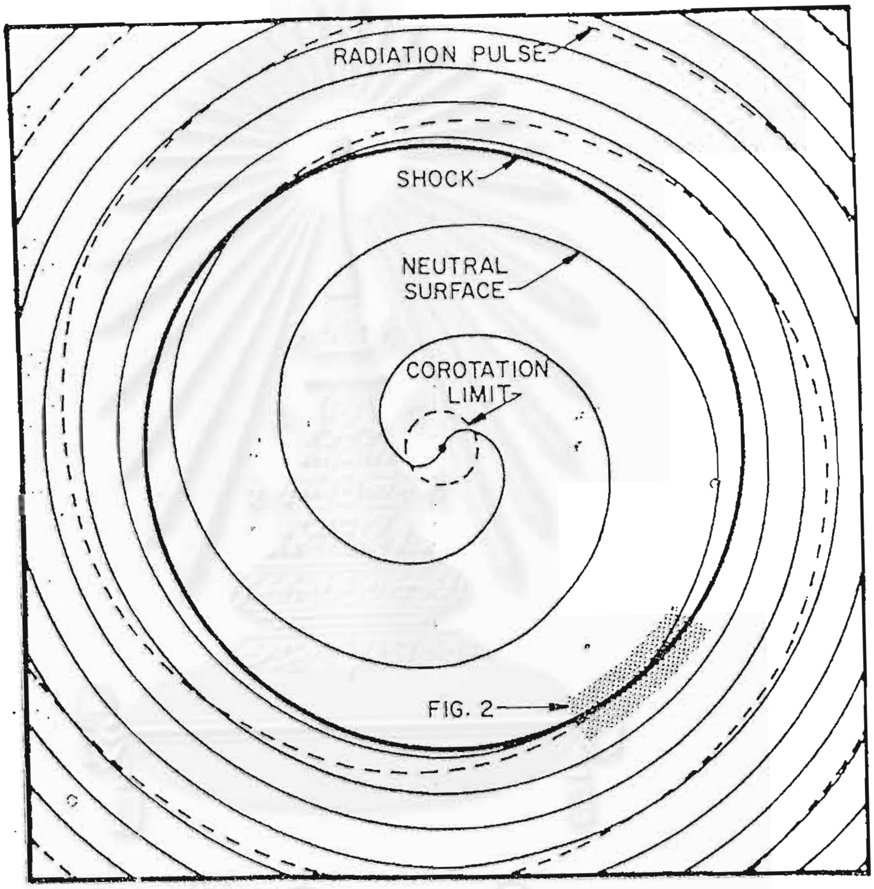
RADIATION PULSE
SHOCK
NEUTRAL SURFACE
COROTATION LIMIT
FIG. 2

Figure 2.6: Magnetic field outside the light cylinder (Michel, 1991).

given the presence of an electromagnetic field or nearby matter (for momentum conservation). These electrons and positrons are accelerated and in turn emit their own energetic photons which create more electron-positron pairs, and so on.

2.2 The Crab Pulsar

The best example for the study of pulsars is the Crab pulsar. The Crab pulsar has many interesting properties. First, this pulsar was discovered in 1054 A.D. by a Chinese astronomer. In this discovery, he found a new star in the sky that never appeared in this position and the brightness of this star was so high that he could see this star by the naked eye. Additionally, the star was still bright for a long time, about 23 days. Really, what the astronomer found was not the Crab pulsar but rather the supernova which later became the Crab pulsar. The reason for being called the Crab nebula, even through it is in Taurus, is its shape like a Crab as Fig. 2.7. The outstanding property of this nebula is its brightness. It is the pulsar nebula most suitable for observation and study of the structure of pulsar nebulae, so we use it as a prototype. The data received in many ways makes studying this pulsar, and this nebula, easier. The data such as the image in the X-ray band of the ROSAT/HRI instrument and in the optical band of the Hubble Space Telescope are useful in the analysis. In particular, the WFPC2 camera of the Hubble Space Telescope is very helpful in modeling the pulsar and its interaction with surrounding nebula. From the studies of the Crab pulsar we can classify the bright regions surrounding the pulsar as in Fig. 2.8.

A **Knot** is a sharp, bright region located at the southeast of the pulsar. In the figure we can see two knots in this direction, where knot 1 is located at 0''.65 and the other, knot 2, is at 3''.8 from the pulsar.

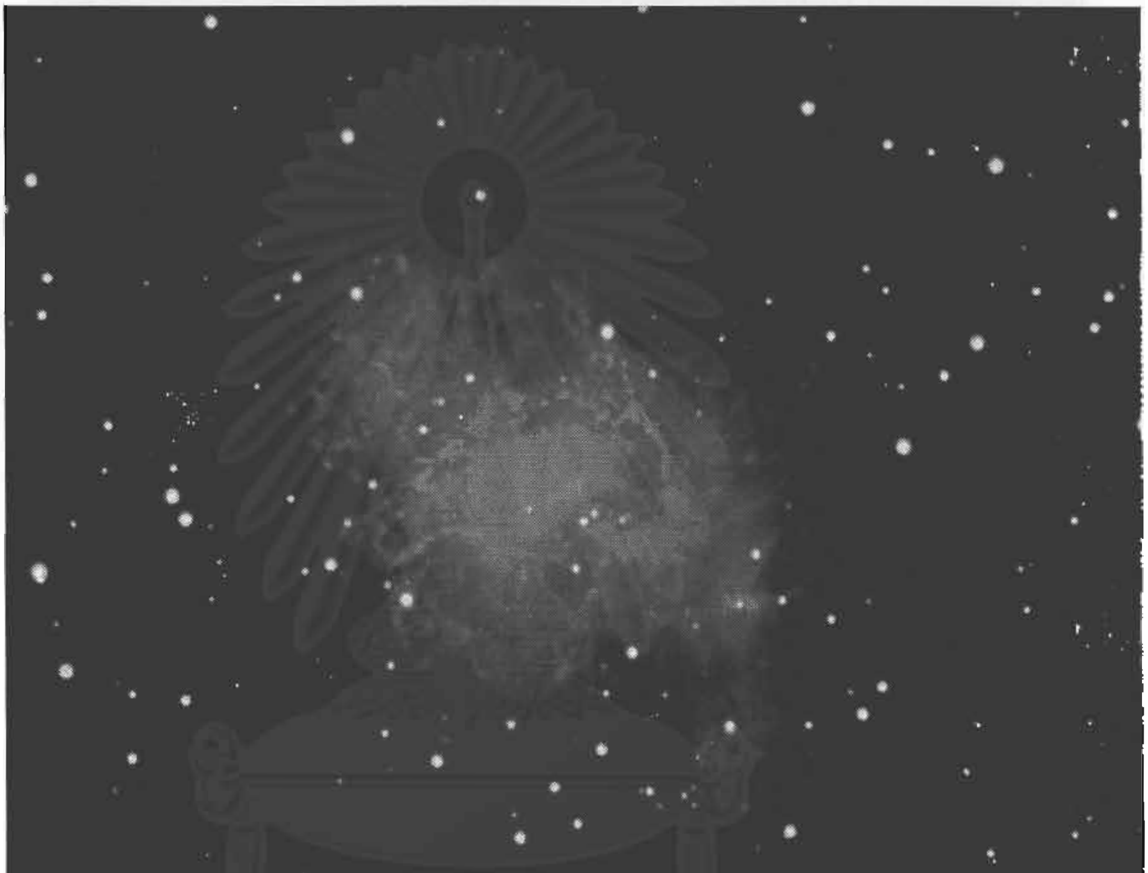

Figure 2.7: The Crab nebula (http://www. seds.org/billa/twn/orig/n1952noao.jpg).

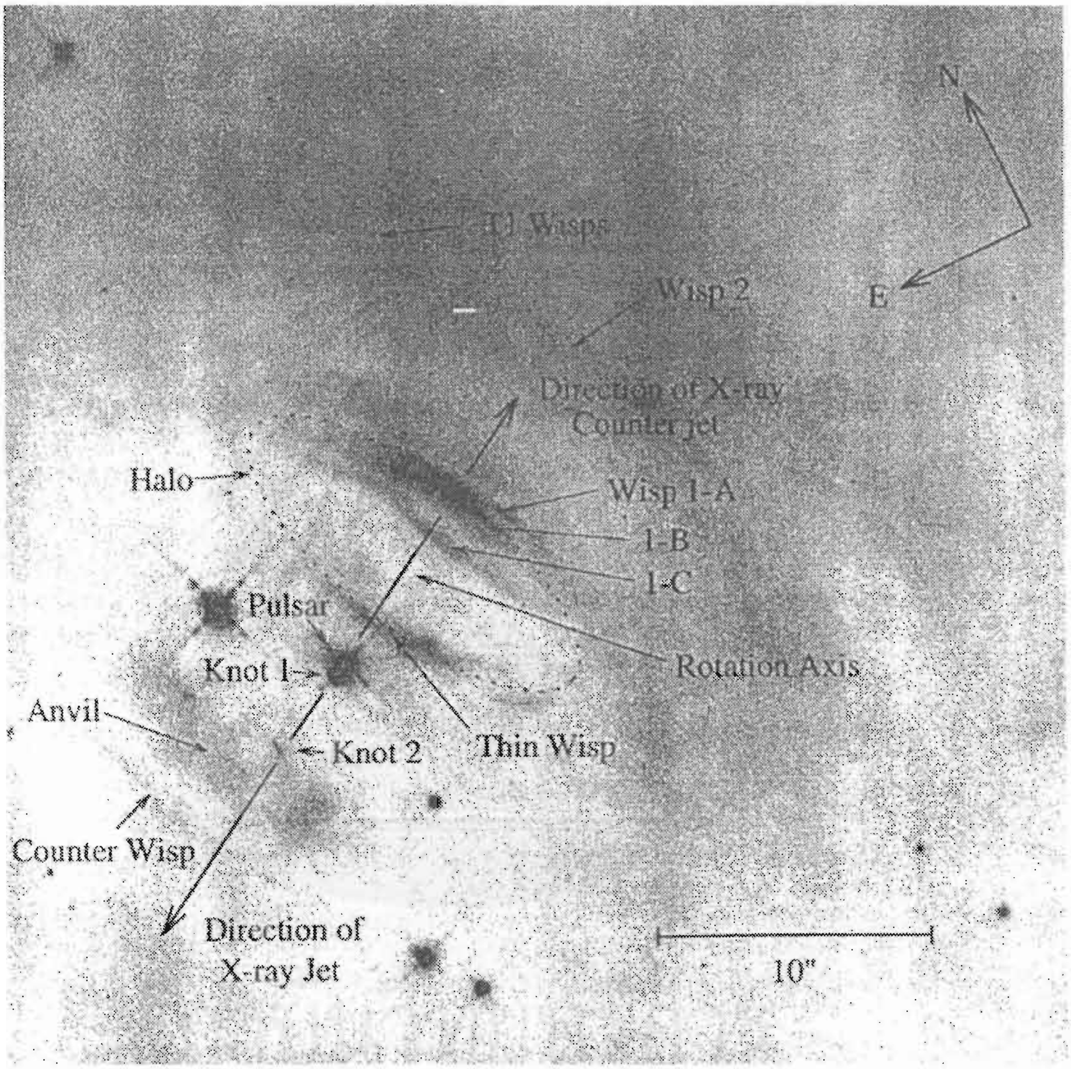
N
E
T1 Wisps
Wisp 2
Direction of X-ray
Counter jet
Halo
Wisp 1-A
1-B
1-C
Pulsar
Rotation Axis
Knot 1
Anvil
Knot 2
Thin Wisp
Counter Wisp
Direction of
X-ray Jet
10"

Figure 2.8: WFPC2 image of the bright region of the Crab pulsar (Hester et al. 1995).

A **Wisp** is a bright region located at the northwest of the pulsar. Wisps are different in each position. Wisp 1 and the Thin Wisp are located at 7".3 and 1".8 from the pulsar, respectively. Wisp 2 is not like first two. It has an amorphous form and is located at 14". The **counter wisp** is located at 8".3 to the southeast of the pulsar. The **anvil** is also amorphous in form but is located between the counter wisp and the pulsar.

2.3 Models of Shocks in the Crab Nebula

One result of the interaction between the pulsar and its surrounding nebula is the shock from the pulsar wind. As we have discussed, the PWTS may be the source of the highest energy galactic cosmic rays of $E \sim 10^{18}$ eV (Bell, 1992; Lucek and Bell, 1994), so the study of the interaction between pulsars and their nebulae is important. Because the Crab pulsar is the prototype of a general pulsar, we will consider the structure of shocks in the Crab nebula. There are many models of the shock in the Crab pulsar. The first was proposed in 1974 (Rees and Gunn, 1974). This model proposed that the shock is located at about 10 per cent of the nebular radius. This estimate of the shock radius is still used and our simulations use this shock radius, too. Aschenbach and Brinkmann (1975) modeled the X-ray structure of the Crab nebula. Their model is shown in Fig. 2.9. As can be seen in Fig. 2.9, the geometry of this model has cylindrical symmetry, whereas the shock model of Rees and Gunn (1974) had spherical symmetry. The limited angular extent may well be accurate; however, in our work we use the simpler model, Rees and Gunn's model. Later models of shocks in the Crab nebula have been concerned with optical or IR features near the Crab pulsar (Gallant and Arons, 1994; Hester et al., 1995). In modeling these features, the model of Aschenbach

หอสมุดกลาง สถาบันวิทยบริการ
จุฬาลงกรณ์มหาวิทยาลัย

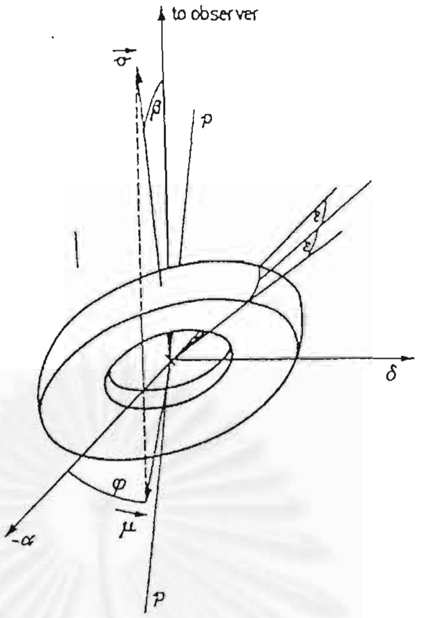

Figure 2.9: The model of the X-ray torus of Aschenbach and Brinkmann (1975).

and Brinkmann is more realistic than the model of Rees and Gunn. Even though the models of optical features orient the shock model in the nearly same direction, there are differences in details of the models, such as those of Gallant and Arons (1994) and Hester et al. (1995).

An important interaction of the pulsar wind and the external magnetic field is by synchrotron radiation of charged particles, especially electrons, which is readily observed from Earth. The bright regions in the Crab nebula mostly consist of light from synchrotron radiation. Now many works try to model the Crab nebula structure, pulsar wind structure, or shock structure via describing the bright regions. The recent work of Gallant and Arons fit their model to a contour plot of the I-band appearance of the inner region of the Crab nebula in optical synchrotron light (Fig. 2.10). From the Crab nebula image of van den Bergh and Prichet (Fig. 2.11), the best-fit parameters of their model of the wind from the Crab pulsar are as in Table 2.2.

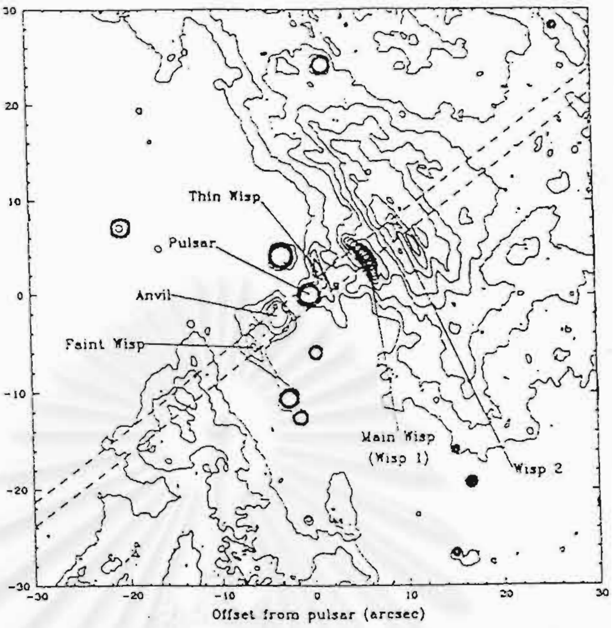

Figure 2.10: A contour plot of an I-band image of the Crab nebula (van den Bergh & Pritchet, 1989 cited by Gallant and Arons, 1994).

WIND PARAMETERS

Parameter	Value
σ	0.003 ± 0.002
$\rho_i \equiv m_i N_{1i}/m_{\pm} N_{1\pm}$	2
γ_1	$(4 \pm 2) \times 10^6$
B_1	$(5.5 \pm 2.5) \times 10^{-5}$ G
θ_i	50°
$\dot{N}_{\pm}$	0.5×10^{38} s^{-1}
$Z\dot{N}_i$	3×10^{34} s^{-1}

Table 2.2: Best-fit wind parameters from the model of Gallant and Arons (1994).

Figure 2.11: Central 100″× 100″ of the Crab nebula with a resolution of 0″.5 from the Canada-France-Hawaii Telescope (van den Bergh and Pritchet, 1989).

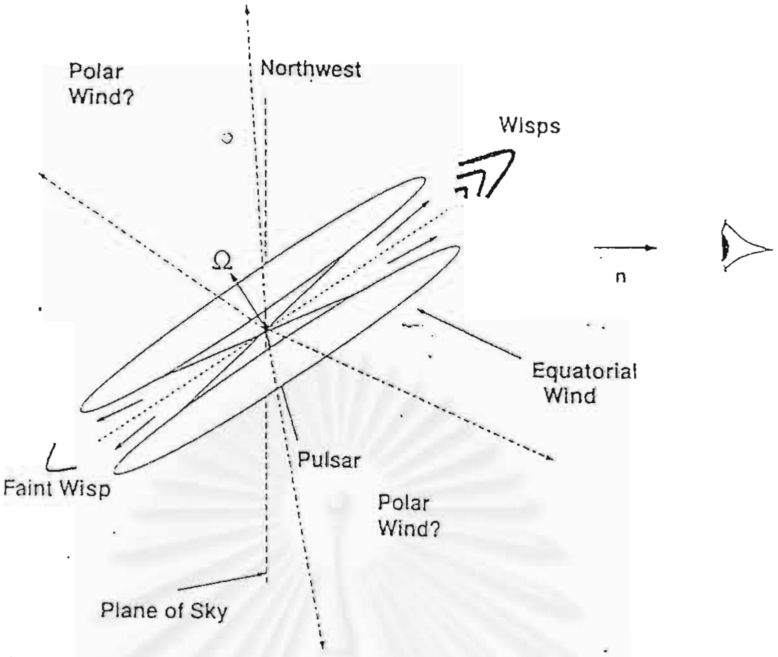

Figure 2.12: Assumed equatorial wind geometry in the model of Gallant and Arons (1994).

In Table 2.2, σ is the ratio between the field energy and particle energy, $\sigma \equiv B^2/(4\pi m N \gamma c^2)$, B is the magnetic field, m is the particle mass, N is the density of particles, γ is the Lorentz factor of the flow, c is the velocity of light, ρ is the ratio of ion to pair energy fluxes, $\rho \equiv N_i A m_p/(N_\pm m_e)$, $N_{i(\pm)}$ is the ion (electron-positron pair) density, A is the atomic number, $m_{p(e)}$ is the mass of the proton (electron), and θ is the angle between the equator of pulsar and the plane of the sky as in Fig. 2.12. On the other hand, the high-resolution observational data from the Hubble Space Telescope show the fine structure of the bright regions (Hester et al, 1995) as in Fig. 2.8. Hester et al. (1995) used these data to model the Crab pulsar wind structure and also the shock structure, in Fig. 2.13 differently from the model of Gallant and Arons. Even through the model of Hester et al. comes from higher resolution data, in our opinion they do not describe the details of the mechanisms in their model. The model comes

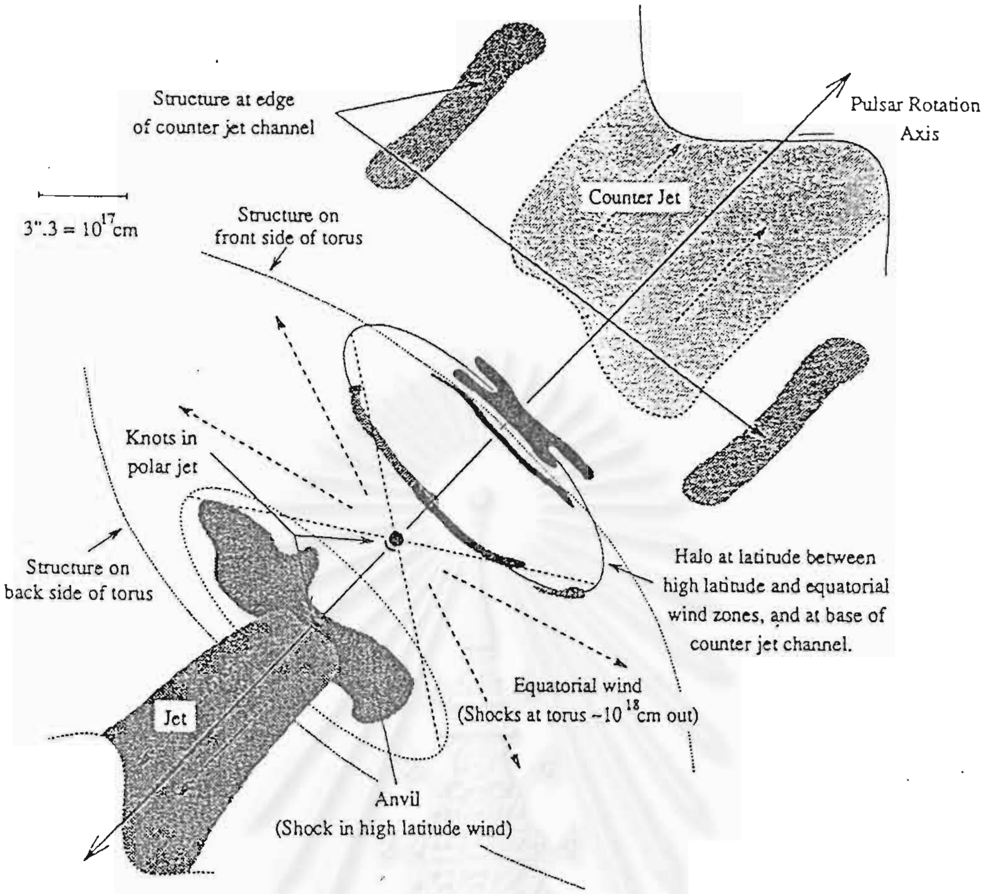
Structure at edge
of counter jet channel
Pulsar Rotation
Axis
Counter Jet
3".3 = 10^{17}cm
Structure on
front side of torus
Knots in
polar jet
Structure on
back side of torus
Halo at latitude between
high latitude and equatorial
wind zones, and at base of
counter jet channel.
Equatorial wind
(Shocks at torus ~10^{18}cm out)
Jet
Anvil
(Shock in high latitude wind)

Figure 2.13: The Crab nebula structure in the model by Hester et al., (1995).

from looking at the data and imagining the structure. Therefore, in our work we choose to use the model of Gallant and Arons via their values for each parameter and the wind structure.

The structure of the magnetic field around the pulsar is also an interesting problem in the study of pulsars. The forms of magnetic field in the far zone and the near zone are quite different. The near zone magnetic structure is a dipole field form in which the poloidal magnetic field dominates. On the other hand, the magnetic field structure in the far zone is dominated by the toroidal magnetic field. and would accumulate in the region $R_s < R < R_{neb}$ (Rees and Gunn, 1974). In some models of the magnetic field there are striped (alternating) magnetic fields (Coroniti, 1990) in the far zone and these magnetic stripes may undergo reconnection and accelerate particles.

Both models have good and bad points in different aspects so we cannot absolutely reject one model and accept the other one.

Chapter 3

Extension of Diffusive Shock Acceleration Theory to a Relativistic, Superluminal Shock

In Chapter 2, we saw that many models about pulsars are concerned with shocks, including pulsar wind termination shocks (PWTS), which might accelerate high energy particles from a pulsar. Because it is a superluminal shock, the mechanisms of acceleration will be different from subluminal shocks, as will be discussed later. Then in this chapter we will present modified mechanisms for a superluminal shock. However, before we discuss these mechanisms we should know the basic idea of the mechanisms of acceleration such as the first-order Fermi mechanism.

3.1 Mechanisms of Accelerating Particles

In the observed data of galactic cosmic rays, the spectrum is in power law form (Fig. 1.1 in chapter 1). Some scientists try to explain this by modeling cosmic rays as a fluid. These cosmic rays can come to us by diffusion through interstellar matter. For this model we can generate an equation describing the distribution of the cosmic rays,

$$\frac{dN(E)}{dt} = \frac{d}{dE}(b(E)N(E)) + Q(E,t) + D\nabla^2 N(E). \tag{3.1}$$

This equation is called the "diffusion-loss equation" (Longair, 1994). Here $N(E)$ is the number density of cosmic rays, $Q(E)$ is the number density of ejected

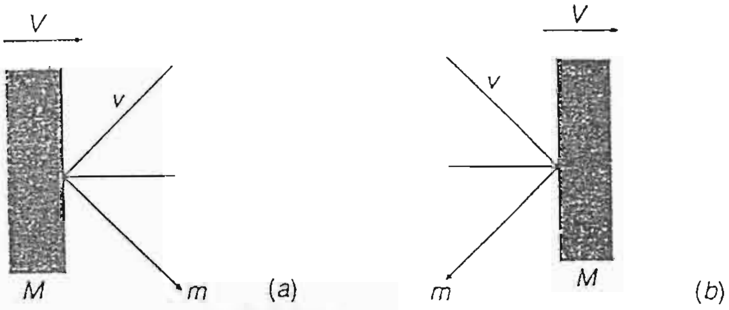

Figure 3.1: Collision between a particle of mass m and a cloud of mass M: (a) A head-on collision, (b) a following collision (Longair, 1994).

cosmic rays, and in the last term of the right side of the equation there is a scalar diffusion coefficient, D. The energy loss/gain parameter, $b(E)$, is an important parameter also, which is defined as

$$b(E) = -\frac{dE}{dt}. \tag{3.2}$$

In the definition we can see that if $b(E)$ is positive the particles lose energy. Particles can lose their energy by many processes such as ionization, bremsstrahlung, adiabatic losses, synchrotron radiation and inverse Compton scattering, and $b(E)$ has a unique form in each process. The idea now known as second-order Fermi acceleration was generated first by Fermi in 1949. Although this idea is no longer believed to account for galactic cosmic rays, it is the seed of the later idea of shock acceleration (first-order Fermi acceleration) of cosmic rays. It is well known that magnetic mirroring will occur when a particle travels in a non-uniform magnetic field. We can treat the magnetic mirroring as an elastic collision with a massive cloud as in Fig. 3.1. For this event we classify two types of collisions. The first is the head-on collision and the second is the following collision. We can show that from a head-on or following collision the particle will gain or lose energy

(Longair, 1994) as

$$\Delta E = E\left[\frac{2Vv\cos\theta}{c^2} + 2\left(\frac{V}{c}\right)^2\right], \tag{3.3}$$

where V is the massive cloud velocity, v is the particle velocity and θ is the angle between the two. For a head-on collision particles will gain energy but the particles will lose energy for a following collision. The head-on collision has more probability than the following collision because of a higher relative velocity, so the particles gain energy on average. The probability of a collision of moving particles depends on θ as $\gamma(1 + \frac{V\cos\theta}{c})$ (Longair, 1994). When we average ΔE, weighted by the probability, over $\cos\theta$ from -1 to 1 we get

$$\frac{\int_{-1}^{1} E\left[\frac{2Vv\cos\theta}{c^2} + 2\left(\frac{V}{c}\right)^2\right]\left[\gamma\left(1 + \frac{V\cos\theta}{c}\right)\right] d\cos\theta}{\int_{-1}^{1}\gamma(1 + \frac{V\cos\theta}{c})d\cos\theta}$$

and in the limit $v \to c$ this equation will give

$$\langle\frac{\Delta E}{E}\rangle = \frac{8}{3}\left(\frac{V}{c}\right)^2. \tag{3.4}$$

Clearly, the particle gains energy to second order in $\frac{V}{c}$. That is why this mechanism is called "second order Fermi acceleration." This mechanism is believed to operate in impulsive solar flares, in which context it is referred to as "stochastic acceleration." Even through this mechanism can explain the power law distribution of galactic cosmic rays, there are some problems with this model, e.g., the random velocities of interstellar clouds in the Galaxy are very small compared with the velocity of light, of order 10^{-4} c and the number of collisions would be roughly one per year.

ศูนย์วิทยทรัพยากร
จุฬาลงกรณ์มหาวิทยาลัย

3.1.1 First-Order Fermi Acceleration

First-order Fermi acceleration is a modified version of the above mechanism. It is developed from the idea of Fermi and used in many ways in astrophysics now.

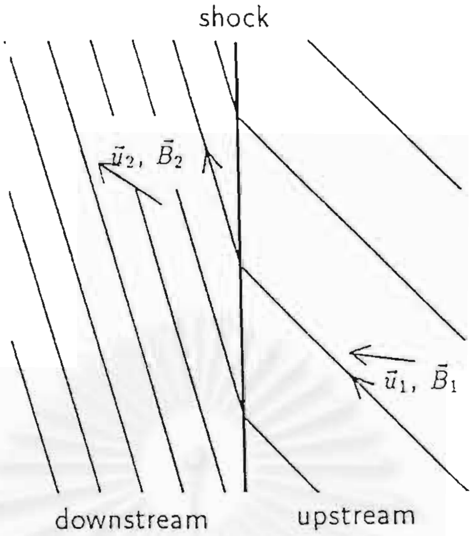

Figure 3.2: Steady state of the shock in the shock rest frame.

There were many people dealing with this mechanism in the late 1970s such as Bell (1978) and Blandford and Ostriker (1978). Shocks, which are defined as discontinuities in the flow velocity, are usually involved with this mechanism as we will discuss later. Let us consider the mechanism of this acceleration. When shocks occur there will be two regions separated by them. They are called "upstream" and "downstream." On both sides of shocks (Fig. 3.2), there are parameters called B_1, v_1, ρ_1 and B_2, v_2, ρ_2, where B is the magnetic field strength, v is the flow velocity, ρ is the mass density, and the subscripts 1 and 2 refer to the upstream and downstream regions, respectively. At a steady state, a flux of high energy particles is assumed to be present both upstream and downstream. Reasonable assumptions are that the velocity of high energy particles is very much greater than the velocity of the shock, and the thickness of the shock front is very small compared to the Larmor radius of particles. Like the second-order Fermi acceleration mechanism, we consider the head-on and following elastic collisions with turbulent magnetic field irregularities. For simplifying the problem

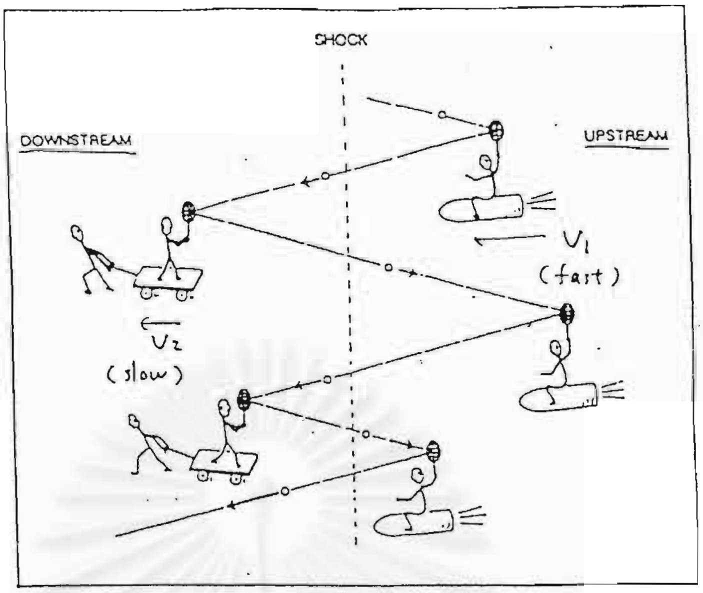

Figure 3.3: Analogy for the acceleration of ions near a shock (Terasawa, 1995).

we consider only the case of direct collisions. This situation can be illustrated as in Fig. 3.3. For the head-on collision, the momentum of particle changes by $\approx 2mV_1$ while the change of momentum of the particle in the following collision $\approx -2mV_2$. Because $V_1 < V_2$, the particle gains momentum in a complete cycle, $\Delta p = 2m(V_1 - V_2) > 0$. The energy gain in a general collision from an oblique shock is (Bell, 1978)

$$E_{k+1} = E_k \left(\frac{1 + \mathrm{v}_{k1} \cdot (\mathrm{V}_1 - \mathrm{V}_2)}{1 + \mathrm{v}_{k2} \cdot (\mathrm{V}_1 - \mathrm{V}_2)} \right), \tag{3.5}$$

where E_k is the k^{th} crossing energy, $v_{k1(k2)}$ is the particle velocity after crossing the shock k times in upstream (downstream) direction, and $V_{1(2)}$ is the flow velocity upstream (downstream). It has been shown (Longair, 1994; Protheroe, 1996) that the average of energy gain is

$$\frac{\Delta E}{E} \propto \frac{V}{c}. \tag{3.6}$$

The energy increase is of first order in V/c. Since usually $V << c$, this is more efficient than the previous mechanism, so this mechanism is called "first-order Fermi acceleration." In this work we consider this acceleration mechanism at shocks, but it can also take place in other situations (Ruffolo and Chuychai, 1999).

3.2 Shocks

In any fluid, if the sources of sound have velocities greater than the velocity of sound waves in such a fluid, the interesting phenomena called a "shock" will occur. When shocks occur there is a discontinuity in the velocity of the flow in space. The discontinuity is caused by a collision between two fluids or between a supersonic fluid and an obstacle which have a supersonic relative velocity. At subsonic velocities, the forward region of a fluid can communicate via waves with the region behind it, which gradually changes its velocity, whereas for a supersonic flow, when the forward region impacts the shock, the region behind will also collide with the same speed and make a compressional discontinuity in the fluid. Such discontinuities are called shock waves. In fact, we can define a shock as a discontinuity of the flow velocity in space. In astrophysics shocks play an important role in acceleration of cosmic rays. In the universe, there are many regions where shocks occur, such as at the edge of the solar system (solar wind termination shock) and at supernova remnants (supernova shocks and pulsar wind termination shocks). We can classify shocks in many ways. However, in this thesis we will classify them into two classes by determining the velocity of intersection of the magnetic field line and the shock wave front. The first category comprises subluminal shocks and the second comprises superluminal shocks.

3.2.1 Subluminal Shocks

When we call a shock subluminal it means that the intersection point of magnetic field lines and the shock front travels with a velocity less than the velocity of light. In astrophysics there are many shocks that can be classified as in subluminal shocks such as solar wind termination shocks and bow shocks.

In Fig. 3.2, the magnetic field is inclined to the flow velocity **v** in both the upstream and downstream regions. In the plasma rest frame, the electric field vanishes because the plasma is a good conductor. Due to the relativistic transformation,

$$\mathrm{E}' = \gamma(\mathrm{E} + \mathrm{v} \times \mathrm{B}), \tag{3.7}$$

where E′ is the electric field in the plasma rest frame and E and B are the electric field and magnetic field in shock rest frame, respectively. Then in the shock rest frame, if **v** is not parallel to **B** there is an electric field

$$\mathrm{E} = -\mathrm{v} \times \mathrm{B}. \tag{3.8}$$

However, there is a special frame in which the electric field disappears. In the de Hoffman-Teller frame (de Hoffman and Teller, 1950), we see that the intersection of the magnetic field and the shock wave front is at rest (Fig. 3.4). Fluid flow from upstream to downstream absolutely must cross the shock.

It is reasonable to use a transport equation to describe the behavior of particles in the fluid flow crossing the shock. For example, Ruffolo (1999) solved a transport equation for a shock in the solar wind. The transport equation which describes the particle transport is (Ruffolo, 1995)

$$\begin{aligned}
\frac{\partial F(t,\mu,z,p)}{\partial t} &= -\frac{\partial}{\partial z}\mu v F(t,\mu,z,p) \\
&\quad -\frac{\partial}{\partial z}\left(1-\mu^2\frac{v^2}{c^2}\right) u F(t,\mu,z,p) \\
&\quad +\frac{\partial}{\partial \mu}\frac{\varphi(\mu)}{2}\frac{\partial}{\partial \mu}\left(1-\mu\frac{uv}{c^2}\right) F(t,\mu,z,p),
\end{aligned} \tag{3.9}$$

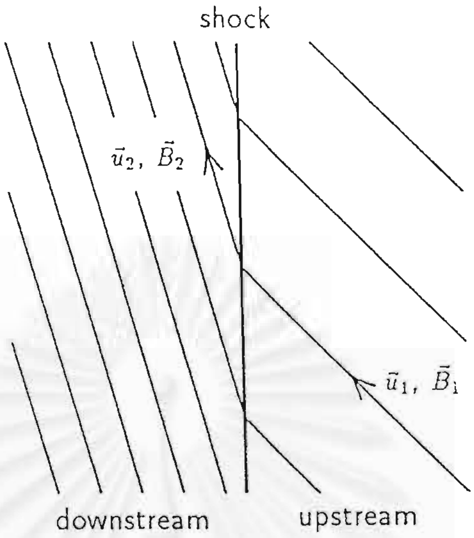

Figure 3.4: Shock in the de Hoffman-Teller frame (Ruffolo, 1999).

where $F \equiv d^3N/dzd\mu dp$ is the density of particles in a given magnetic flux tube,

t is the time in the shock frame,

μ is the pitch angle cosine in the wind frame,

z is the distance from the shock along the magnetic field in the de Hoffman-Teller or shock frame,

p is the particle momentum in the wind frame,

v is the particle velocity in the wind frame,

u is the solar wind speed along the magnetic field in the shock frame, and

φ is the pitch angle scattering coefficient.

In this transport equation we can identify each term on the right hand side. The first term accounts for the effect of streaming, the second term is for convection by the wind, and the effect of pitch angle scattering is in the third term. Note that, for convenience (Kirk, 1994), F is in a so-called mixed frame where momentum space variables (e.g., μ and p) are defined in the wind frame and z and

t are in the shock frame. In addition to the transport equation, which applies on either side of the shock, we must use special conditions describing how particles cross the shock; for example, at an oblique shock the particles may be reflected or transmitted by the shock, depending on their pitch and gyrophase angles.

We also need conditions relating the fluid flow on either side of the shock, called Rankine-Hugoniot conditions. These conditions come from the conservation of mass, momentum, and energy. For simplicity, consider the fluid flow to be parallel to the shock normal. The first condition,

$$\rho_1 v_1 = \rho_2 v_2, \tag{3.10}$$

comes from the conservation of mass. The next condition comes from the conservation of momentum, i.e., with a non-divergent momentum flux:

$$\rho_1 v_1^2 + \frac{B_1^2}{8\pi} + p_1 = \rho_2 v_2^2 + \frac{B_2^2}{8\pi} + p_2, \tag{3.11}$$

where $p_1 (p_2)$ is the pressure upstream (downstream). Note that the terms in the momentum flux have units of pressure or energy, and represent the ram pressure, magnetic field pressure, and plasma pressure, respectively. The final condition is the conservation of energy, i.e., equality of the energy flux on either side.

$$\frac{1}{2} v_1^2 + \frac{\Gamma}{\Gamma - 1}\frac{p_1}{\rho_1} + \frac{B_1^2}{8\pi\rho_1} = \frac{1}{2} v_2^2 + \frac{\Gamma}{\Gamma - 1}\frac{p_2}{\rho_2} + \frac{B_2^2}{8\pi\rho_2}, \tag{3.12}$$

where Γ is the adiabatic index (ratio of specific heats). Note that here we have divided both sides of Eq. 3.12 by the mass flux. By using the transport equation and Rankine-Hugoniot conditions, we can solve the problem as in Ruffolo (1999).

In the superluminal case we will modify this transport equation and the Rankine-Hugoniot conditions.

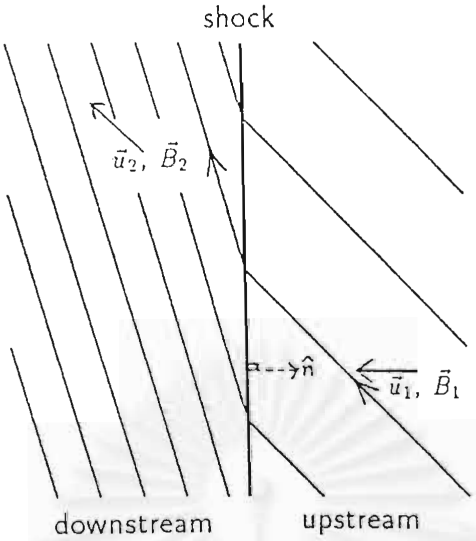

Figure 3.5: Shock in the normal incidence frame.

3.2.2 Superluminal Shocks

In this case the shock wave front travels with a speed near that of light, or the magnetic field is very nearly perpendicular to the shock. Due to this event, we cannot use the simplifying de Hoffman-Teller frame, as in the previous section. The situation of the shock in Fig. 3.2 shows that the intersection of the magnetic field and shock wave front travels with speed $v \sec\theta'$. Note that this is merely a mathematical point; we are not implying that any physical object travels with $v > c$. When this intersection point travels with a speed greater than that of light, we then call it a superluminal shock. Even through we cannot use the de Hoffman-Teller frame, there are many frames of reference that we can use, such as the normal incidence frame as in Fig. 3.5.

Because we changed frames of reference and this case is a relativistic case, we must modify our transport equation and Rankine-Hugoniot conditions. This task is based on the assumption that first-order Fermi acceleration mechanism still works at a superluminal shock, which may well be true in certain astrophysical situations, but in general needs to be checked (see Chapter 4).

3.3 Modified Transport Equation and Rankine-Hugoniot Conditions

3.3.1 Modified Transport Equation

We will derive the modified transport equation from a Fokker-Planck equation for the transport of energetic particles in the interplanetary magnetic field (Ruffolo, 1995):

$$\begin{aligned}\frac{\partial F(t,\mu',z,p')}{\partial t} &= -\frac{\partial}{\partial z}\left(\frac{\Delta z}{\Delta t}F\right)\\ &\quad -\frac{\partial}{\partial \mu'}\left(\frac{\Delta \mu'}{\Delta t}F\right)\\ &\quad +\frac{\partial}{\partial \mu'}\left[\frac{\varphi'(\mu',p')}{2}\frac{\partial}{\partial \mu'}\left(\frac{E'}{E}F\right)\right]\\ &\quad -\frac{\partial}{\partial p'}\left(\frac{\Delta p'}{\Delta t}F\right), \qquad (3.13)\end{aligned}$$

where $\varphi'(\mu',p')$ is the pitch-angle scattering coefficient, the distribution function F is given by

$$F(t,\mu',z,p') = \frac{d^3N}{dz\,d\mu'\,dp'},$$

where N represents the number of particles inside a given flux tube, and Δz, $\Delta\mu'$, and $\Delta p'$ represent the mean change in each quantity over a time Δt. The transport equation in the subluminal case as in Eq. 3.9 is also developed from Eq. 3.13. Here primed variables are in the wind frame. Now it will be modified for the superluminal case in this section. We will first consider the streaming term alone. From Eq. 3.9, selecting only the streaming term leads to

$$\frac{\partial f}{\partial t} = -\mu v\frac{\partial f}{\partial z}, \qquad (3.14)$$

where

$$f \equiv \frac{d^6N}{d^3x d^3p}$$

is the phase space density of particles in either the shock frame or the wind frame. Transforming Eq. 3.14 from the shock frame to the wind frame via the relation (Earl, 1984), we get

$$\left(\frac{\partial f}{\partial t'} + \mu' v' \frac{\partial f}{\partial z'}\right) = \frac{E}{E'}\left(\frac{\partial f}{\partial t} + \mu v \frac{\partial f}{\partial z}\right). \tag{3.15}$$

As in the subluminal shock case, it is convenient (especially for numerical evaluation) to solve for the density of particles in the mixed frame. Thus we consider the relation between phase space in the shock and wind frames according to the Lorentz transformation. Basically, the volume of phase space must be invariant under a Lorentz transformation,

$$d^3q d^3p = d^3q' d^3p'.$$

Phase space in the shock frame transforms to phase space in the mixed frame (with position in the shock frame and momentum in the wind frame) as

$$\frac{d^3q d^3p}{E} = \frac{d^3q \, d^3p'}{E'}.$$

Using the definition of the phase space density, f, we find

$$f = \frac{E'}{E} f^\star,$$

where $f^\star$ is the phase space density in the mixed frame. From Eq. 3.15 and Eq. 3.3.1 we get

$$\frac{\partial f}{\partial t'} + \mu' v' \frac{\partial f}{\partial z'} = \frac{\partial f^\star}{\partial t} + \mu v \frac{\partial f^\star}{\partial z}. \tag{3.16}$$

Now we can write a relativistic transport equation, with only a streaming term, in the mixed frame:

$$\frac{\partial f^\star}{\partial t} + \mu v \frac{\partial f^\star}{\partial z} = 0.$$

If we consider straight magnetic field lines, as in Fig. 3.2 , then f^* can be replaced by F at this point. The main reason that we use the mixed frame with momentum in the wind frame is to write the scattering term in a simple form (Kirk, 1994; Ruffolo, 1995). For this case we can add a scattering term (Earl, 1984):

$$\frac{\partial F}{\partial t} + \mu v \frac{\partial F}{\partial z} = \frac{1}{2} \frac{\partial}{\partial \mu'} \varphi'(p', \mu') \frac{\partial}{\partial \mu'} \frac{E'}{E} F. \tag{3.17}$$

To simplify, we approximate that the magnetic fields on both sides of shock, upstream and downstream, are uniform. That means there are no focusing terms in the transport equation on either side of the shock and the second term in Eq. 3.13 must vanish. Furthermore, there is no acceleration or deceleration except at the shock. This leads to the vanishing of the last term on the right hand side of Eq. 3.13. Next, the second term on the left hand side of Eq. 3.17 needs to be adjusted. In Eq. 3.13 this term, the first term on the right hand side, described the speed of the guiding centers of the particles along the z-direction. In our case the z-direction is parallel to the normal of the shock front. Hence,

$$\frac{\Delta z}{\Delta t} = \mu v \cos\theta, \tag{3.18}$$

where θ is the angle between the magnetic field and the shock normal. Moreover, we must tranform $\mu v \cos\theta$ from the shock frame to the mixed frame. In changing this variable we cannot use a Galilean transformation, but rather must use a Lorentz transformation. Guiding center velocities of particles in the shock frame can be found in this way. From the relation

$$\mu v \cos\theta = v_{||} = \frac{p_{||} c^2}{E}, \tag{3.19}$$

transforming p and E to the mixed frame by Lorentz transformations yields a velocity in the mixed frame of

$$\frac{p_{||} c^2}{E} = c \frac{p'_{||} c + \beta E'}{E' + \beta p'_{||} c}$$

$$
\begin{aligned}
&= \frac{p'_{\|}c^2/E' + \beta c}{1 + \beta p'_{\|}c/E'} \\
&= \frac{\mu' v' \cos\theta + u}{1 + \beta p'_{\|}c/E} \\
&= \left(\frac{\gamma E'}{E}\right)(\mu' v' \cos\theta' + u). \qquad (3.20)
\end{aligned}
$$

Now our transport equation is in the form

$$
\frac{\partial F}{\partial t} + \gamma\frac{E'}{E}(\mu' v' \cos\theta' + u)\frac{\partial F}{\partial z} = \frac{\partial}{\partial \mu'}\frac{\varphi'(p',\mu')}{2}\frac{\partial}{\partial \mu'}\left(\frac{E'}{E}F\right). \qquad (3.21)
$$

This is our modified transport equation. This equation can be used in both upstream and downstream regions.

3.3.2 Modified Rankine-Hugoniot Conditions

We can use the modified transport equation, from the last subsection, to describe flows on both sides of shock. However, the problem at the shock front cannot be solved via the transport equation alone. Additional tools for solving this problem are Rankine-Hugoniot conditions. Since this is a superluminal shock, non-relativistic Rankine-Hugoniot conditions are not adequate. Thus this subsection is concerned with the modification of non-relativistic Rankine-Hugoniot conditions to relativistic Rankine-Hugoniot conditions.

For the relativistic case, it is necessary to use the "energy-momentum-stress" tensor (Landau and Lifshitz, 1963), which is a symmetric tensor,

$$
T = \begin{bmatrix} T_{00} & T_{01} & T_{02} & T_{03} \\ T_{10} & T_{11} & T_{12} & T_{13} \\ T_{20} & T_{21} & T_{22} & T_{23} \\ T_{30} & T_{31} & T_{32} & T_{33} \end{bmatrix} \qquad (3.22)
$$

to derive the modified conditions. T_{00} is the energy density. T_{0i}, when i runs from 1 to 3, is the energy flux density in the i^{th} direction. T_{i0} is the i^{th} component of the momentum density. T_{ij}, when i and j run from 1 to 3, is the flux density of the i^{th} component of the momentum density in the j^{th} direction, or the three-dimensional stress tensor (Goldstein, 1980).

There are some relevant conventions about tensors. When there are two repeated indices there is an implied sum and indices run from 0 to 3,

$$\begin{aligned} a_i b_i &\equiv \sum_i a_i b_i \\ &= a_0 b_0 + a_1 b_1 + a_2 b_2 + a_3 b_3 \end{aligned} \tag{3.23}$$

We consider this problem in the steady state in which the conditions

$$\frac{\partial T_{ij}}{\partial x_j} = 0 \tag{3.24}$$

are satisfied. These conditions lead us to the modified Rankine-Hugoniot conditions. Our problem, now, is to find each element of the tensor, T, in the shock frame. A simple way is to find the elements of the tensor in the co-moving frame and transform them to the shock frame by Lorentz transformation matrices.

Before we find the value of the elements of the tensor, we set another notational convention. Primed variables are the variables in the co-moving frame and unprimed variables are the variables in the shock frame. The variables that have subscript 1 (2) are the variables upstream (downstream). A specific example of such shocks is the PWTS, which is a perpendicular shock in many models. Then we will find modified Rankine-Hugoniot conditions in the perpendicular case and fortunately the paper of de Hoffman and Teller (1950) has discussed this. We will follow their method in finding the modified conditions.

To coincide with the modified transport equation, we choose the perpendicular shocks propagating in the z-direction and the magnetic field in the x-direction. Owing to the infinite value of the conductivity, all electric fields vanish in the primed frame. We define the quantity η' as the relativistic energy density for the primed system:

$$\eta' c^2 = \rho'(m_0' c^2 + E'), \tag{3.25}$$

where ρ' is the density of particles, m_0' is the average rest mass, and E' is the excess energy per particle over and above the rest energy. The momentum-energy-stress tensor in the primed frame is then

$$T' = \begin{bmatrix} \eta' c^2 + \frac{H'^2}{8\pi} & 0 & 0 & 0 \\ 0 & p' - \frac{H'^2}{8\pi} & 0 & 0 \\ 0 & 0 & p' + \frac{H'^2}{8\pi} & 0 \\ 0 & 0 & 0 & p' + \frac{H'^2}{8\pi} \end{bmatrix}. \tag{3.26}$$

Next we transform the tensor in the primed frame to the unprimed frame, the shock frame, by using the Lorentz transformation matrix, Λ, which is, in this situation,

$$\Lambda = \begin{bmatrix} \gamma & 0 & 0 & -\beta\gamma \\ 0 & 1 & 0 & 0 \\ 0 & 0 & 1 & 0 \\ -\beta\gamma & 0 & 0 & \gamma \end{bmatrix}. \tag{3.27}$$

Thus we get the tensor in the unprimed frame:

$$T = \begin{bmatrix} \dfrac{\eta' + \frac{v^2}{c^2}p' + \frac{H'^2}{8\pi}(1 + \frac{v^2}{c^2})}{1 - \frac{v^2}{c^2}} & 0 & 0 & -\dfrac{v\eta' + \frac{v}{c^2}p' + \frac{v}{c^2}\frac{H'^2}{4\pi}}{1 - \frac{v^2}{c^2}} \\ 0 & p' - \frac{H'^2}{8\pi} & 0 & 0 \\ 0 & 0 & p' + \frac{H'^2}{8\pi} & 0 \\ -\dfrac{v\eta' + \frac{v}{c^2}p' + \frac{v}{c^2}\frac{H'^2}{4\pi}}{1 - \frac{v^2}{c^2}} & 0 & 0 & \dfrac{\eta' v^2 + p' + \frac{H'^2}{8\pi}(1 + \frac{v^2}{c^2})}{1 - \frac{v^2}{c^2}} \end{bmatrix}. \tag{3.28}$$

This tensor will hold on both sides of the shock. When upstream (downstream), all quantities are given the subscript 1 (2). In the steady state the four divergences of the tensor vanish as in Eq. 3.24. Since the flow depends only on the z coordinate, we know that $\partial/\partial x$ and $\partial/\partial y$ derivatives are zero, and since the shock system is stationary, the $\partial/\partial t$ derivative is zero. Hence the non-trivial equations are $\partial T_{33}/\partial z = 0$ and $\partial T_{30}/\partial z = 0$. This statement continues to hold across the shock discontinuity. Then we find the energy-momentum stress tensor both upstream, T_1, and downstream, T_2, and consider only 33 and 30 components. We obtain

$$\frac{\eta_1' v_1^2 + p_1' + \frac{H_1'^2}{8\pi}(1 + \frac{v_1^2}{c^2})}{1 - \frac{v_1^2}{c^2}} = \frac{\eta_2' v_2^2 + p_2' + \frac{H_2'^2}{8\pi}(1 + \frac{v_2^2}{c^2})}{1 - \frac{v_2^2}{c^2}} \tag{3.29}$$

and

$$\frac{v_1 \eta_1' + \frac{v_1}{c^2} p_1' + \frac{v_1}{c^2} \frac{H_1'^2}{4\pi}}{1 - \frac{v_1^2}{c^2}} = \frac{v_2 \eta_2' + \frac{v_2}{c^2} p_2' + \frac{v_2}{c^2} \frac{H_2'^2}{4\pi}}{1 - \frac{v_2^2}{c^2}}. \tag{3.30}$$

An additional equation is obtained from the conservation of particles

$$\frac{\rho_1' v_1}{\sqrt{1 - \frac{v_1^2}{c^2}}} = \frac{\rho_2' v_2}{\sqrt{1 - \frac{v_2^2}{c^2}}}. \tag{3.31}$$

Here H_1 and H_2 are related by virtue of the fact that we have assumed the particles to be attached to the magnetic force lines. Thus, the density of magnetic force lines is proportional to the density of particles and we have

$$\frac{H_1'}{\rho_1'} = \frac{H_2'}{\rho_2'}. \tag{3.32}$$

Due to this relation and the conservation of particles we have

$$\frac{H_1' v_1}{\sqrt{1 - \frac{v_1^2}{c^2}}} = \frac{H_2' v_2}{\sqrt{1 - \frac{v_2^2}{c^2}}}. \tag{3.33}$$

We introduce the energy density η in the unprimed system

$$\eta = \frac{\eta'}{1 - \frac{v^2}{c^2}} \tag{3.34}$$

and define the auxiliary quantity

$$p = \frac{p'}{1 - \frac{v^2}{c^2}}. \tag{3.35}$$

Using Eqs. 3.33, 3.34 and 3.35 we can simplify Eqs. 3.29 and 3.30 to the unprimed variables,

$$\eta_1 v_1^2 + p_1 + \frac{H_1^2}{8\pi} = \eta_2 v_2^2 + p_2 + \frac{H_2^2}{8\pi} \tag{3.36}$$

and

$$\eta_1 v_1 + \frac{v_1 p_1}{c^2} + \frac{v_1 H_1^2}{c^2 4\pi} = \eta_2 v_2 + \frac{v_2 p_2}{c^2} + \frac{v_2 H_2^2}{c^2 4\pi}. \tag{3.37}$$

The modified Rankine-Hugoniot conditions in the superluminal case are Eqs. 3.31, 3.36, and 3.37. Another condition that we use is Eq. 3.33. We use these equations for flow across superluminal shocks.

Chapter 4

Simulation Results for a Relativistic, Quasi-Perpendicular, Superluminal Shock

In this chapter we discuss our simulation results. We simulate the trajectory of protons from the pulsar through the PWTS. The reason for these simulations is that we expect that a possible explanation for high energy galactic cosmic ray acceleration could be particle drift from the equator to the poles of the shock which (presumably) has an approximately spherical geometry (see, for example, Bell, 1992; Lucek and Bell, 1994). The parameters used in this simulation mainly follow the model of Gallant and Arons (1994). In addition to addressing the shock crossings of a proton, these simulations will tell us about the applicability of our modified transport equation in Chapter 3.

4.1 Formulation

The situation we consider is for a proton ejected from a pulsar which passes the shock, especially at the equatorial region (Aschenbach and Brinkmann, 1975; Gallant and Arons, 1994). The wind flows with $\gamma \approx 4 \times 10^6$ through the shock which is located at about 10% of the nebula radius (Coroniti, 1990; Bell, 1992; Begelman, 1998). The toroidal magnetic field strength upstream is approximately $B_1 \approx 5 \times 10^{-5}$ G.

In the situation we simulate, the value of Lorentz factor is high. Hence, it is reasonable that for computing $d\mathrm{x}/dt$, we will approximate the velocity of the particle to be c. The velocity $v = c(1 - \frac{1}{\gamma^2})^{1/2}$ is, for $\gamma > 10^6$, indistinguishable from c in the presence of computational round-off error. Consequently, in the equations used in the simulation, we suggest using $\mathbf{v} = c(\mathbf{p}/p)$. The set of equations we use in this simulation is

$$
\begin{aligned}
\dot{x} &= \frac{p_x}{\sqrt{p_x^2 + p_y^2 + p_z^2}}c, \\
\dot{y} &= \frac{p_y}{\sqrt{p_x^2 + p_y^2 + p_z^2}}c, \\
\dot{z} &= \frac{p_z}{\sqrt{p_x^2 + p_y^2 + p_z^2}}c
\end{aligned}
\tag{4.1}
$$

for position and

$$
\begin{aligned}
\dot{p_x} &= q(\mathrm{v} \times \mathrm{B})_x + qE_x, \\
\dot{p_y} &= q(\mathrm{v} \times \mathrm{B})_y + qE_y, \\
\dot{p_z} &= q(\mathrm{v} \times \mathrm{B})_z + qE_z
\end{aligned}
\tag{4.2}
$$

for momentum. For the magnetic field structure we use

$$\mathrm{B} = B_\phi \mathrm{e}_\phi, \tag{4.3}$$

where B is the magnetic field that averaged over the pulsar rotation and

$$
B_\phi = \begin{cases} \dfrac{B_0 R_s \sin\theta}{r} & r < R_s \\[2ex] \dfrac{3B_0 R_s \sin\theta}{r} & r \geq R_s \end{cases} \tag{4.4}
$$

$$\mathbf{u} = u\mathbf{e}_\mathbf{r} \tag{4.5}$$

$$u = \begin{cases} c & r < R_s \\ c/3 & r \geq R_s \end{cases} \tag{4.6}$$

and

$$\mathrm{E} = -\mathbf{u} \times \mathrm{B}, \tag{4.7}$$

where

E is the electric field,

B is the magnetic field,

u is the wind velocity,

R_s is the shock radius, about 5×10^{15}m,

r is the distance from the pulsar, and

θ is the polar angle.

Note that for simplicity we neglect the reversal of the B direction for $\theta < 90^\circ$, and we try to work only in the northern hemisphere.

We use Eqs. 4.2 and 4.3 in simulating the trajectory of the particle. These sets of equations are differential equations so we choose the adaptive step-size Runge-Kutta method (Press et al., 1988) to solve them. On the other hand, before we used results from this program we tested it for simple conditions for which we can find analytic solutions as follows. The first condition we used to test the program was the simplest one in which the particle was in a uniform magnetic field. In this example we used an initial $p_x = 1.92 \times 10^{-12}$ kg m/s ($\gamma = 4 \times 10^6$), $B_y = 1.0 \times 10^{-8}$ T and other variables were set to zero. Under these conditions we know that the particle has a circular orbit with gyroradius

$$\begin{aligned} R_g &= \frac{p}{qB} \\ &= \frac{1.92 \times 10^{-12}\ \mathrm{kg\ m/s}}{(1.6 \times 10^{-19}\mathrm{C})(1.0 \times 10^{-8}\mathrm{T})} \\ &= 1.2 \times 10^{15}\mathrm{m}. \end{aligned}$$

This value coincides with the result of the simulation as in Fig. 4.1. In the next test case, we added a wind velocity only in the x direction, $u_x = 1.0 \times 10^{-8}$ m/s, to the previous case. Consequently, the electric field due to the plasma flow is

$$E_z = -u_x B_y. \tag{4.8}$$

The result of this program is shown in Fig. 4.2. This result coincides with the analytic solution. When the program passed the test, we used this program to

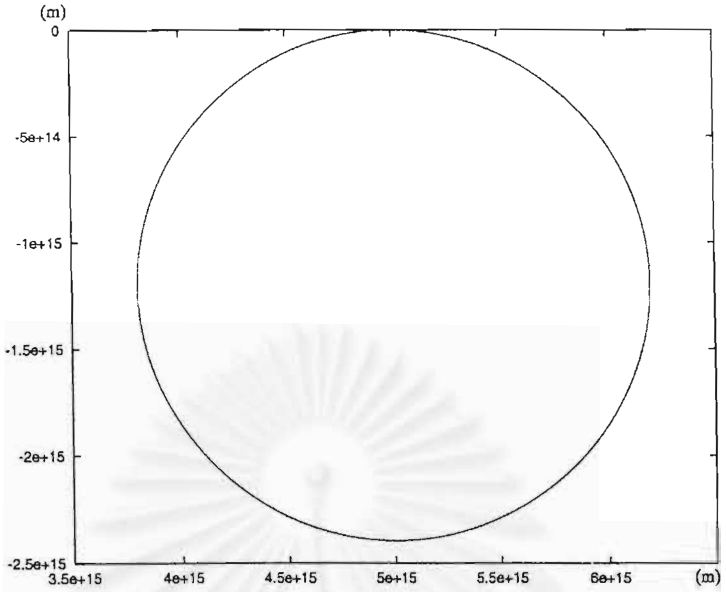

Figure 4.1: A test of the program: motion of a particle in a uniform magnetic field.

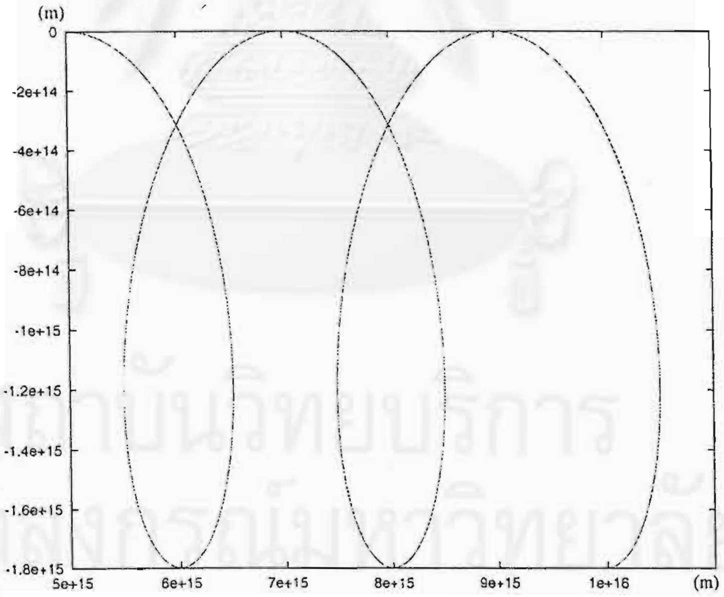

Figure 4.2: The motion of the particle in a uniform magnetic and electric field.

simulate the situation described above. The program is shown in Appendix A.

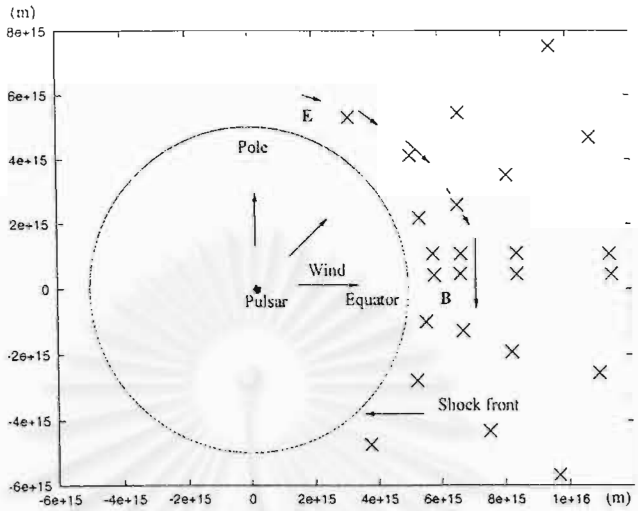
(m)
8e+15
6e+15
4e+15
2e+15
0
-2e+15
-4e+15
-6e+15
-6e+15
-4e+15
-2e+15
0
2e+15
4e+15
6e+15
8e+15
1e+16
(m)
E
Pole
Wind
Pulsar
Equator
B
Shock front

Figure 4.3: The situation used in the simulation.

4.2 Results

In this section we show the results of the program. In the simulations we choose a proton injected near the shock radius, $R_{shock} \approx 5\times10^{15}$ m, with a momentum near the momentum that coincides with the wind Lorentz factor at a latitude above the equatorial plane by about 10 degrees, coinciding with the upper latitude in the model of Aschenbach and Brinkmann (1975). Fig. 4.3 shows the situation in our simulation and we see that there is an electric field due to the pulsar wind cross the magnetic field in the direction from the North pole to the equator. Again, note that for simplicity we neglect the reversal of B for $\theta > 90°$, and we work in the northern hemisphere. Now these are the results of the simulations:

Our simulations show that in most cases, particles do not cross the shock again after the first crossing. There are some momentum values, such

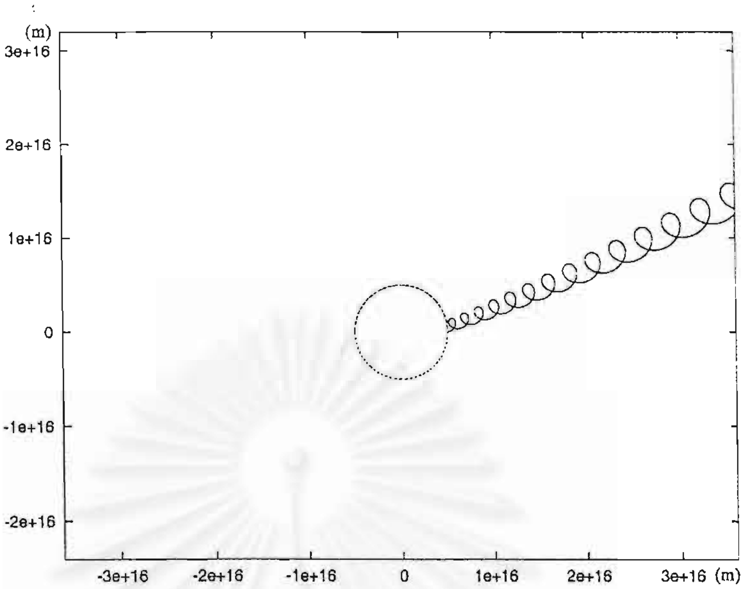

Figure 4.4: The result for momentum 1.92×10^{-12} kg m/s ($\gamma = 4 \times 10^6$).

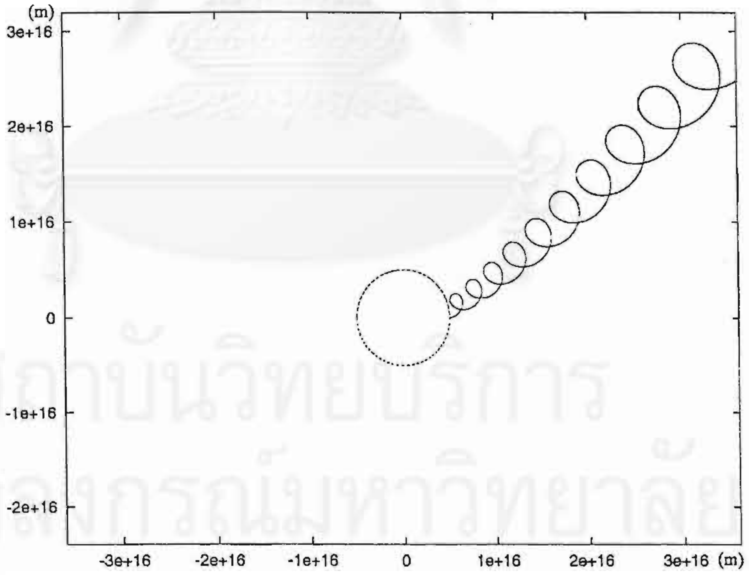

Figure 4.5: The result for momentum 2.92×10^{-12} kg m/s ($\gamma \approx 5.82 \times 10^6$).

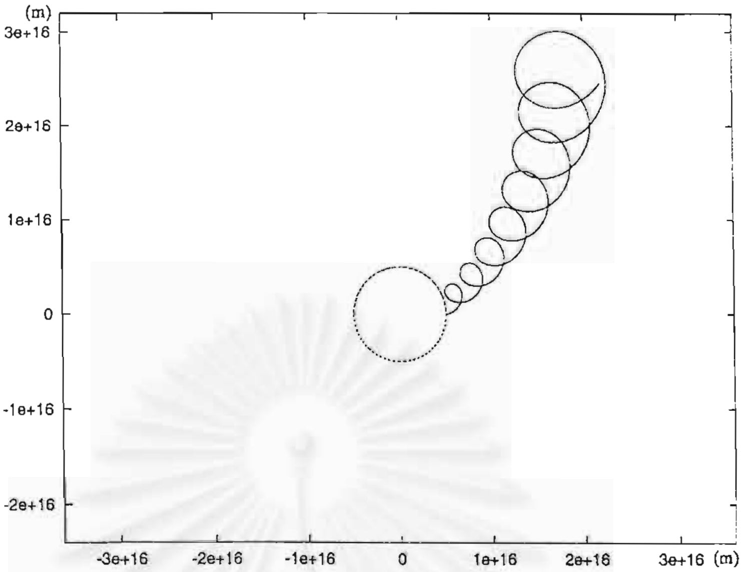

Figure 4.6: The result for momentum 3.44×10^{-12} kg m/s ($\gamma \approx 6.85 \times 10^{6}$).

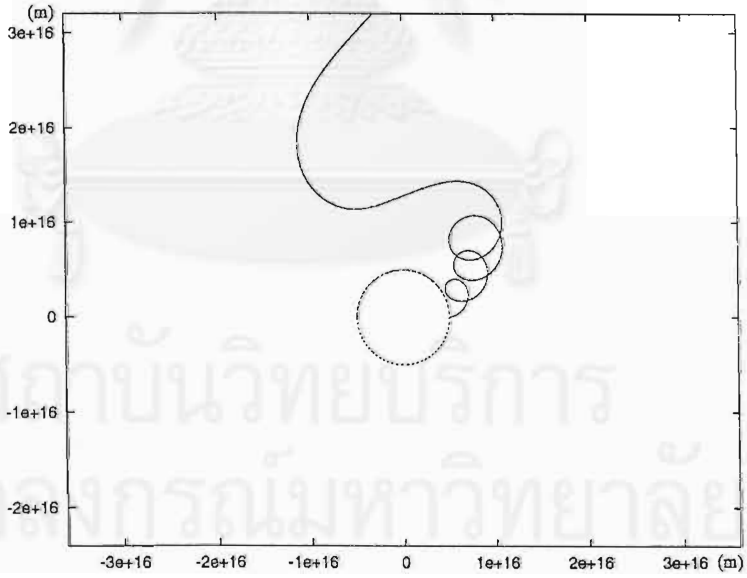

Figure 4.7: The result for momentum 3.92×10^{-12} kg m/s ($\gamma \approx 7.81 \times 10^{6}$).

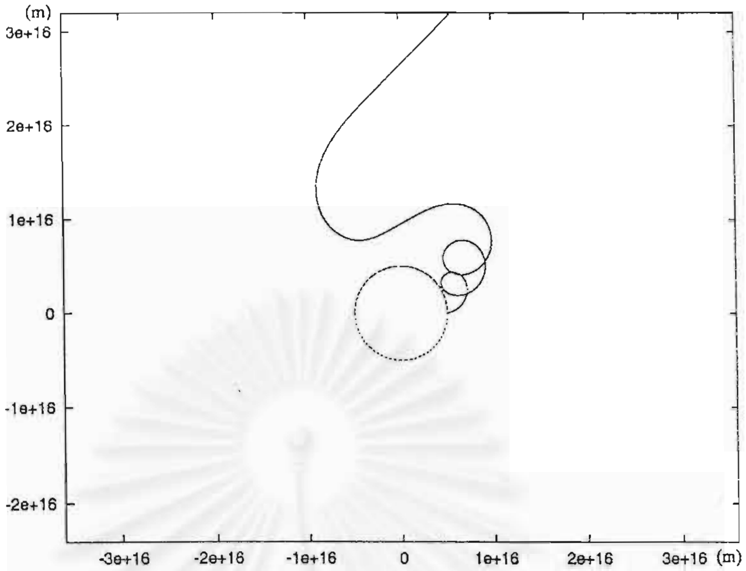

Figure 4.8: The result for momentum 4.10×10^{-12} kg m/s ($\gamma \approx 8.71 \times 10^{6}$).

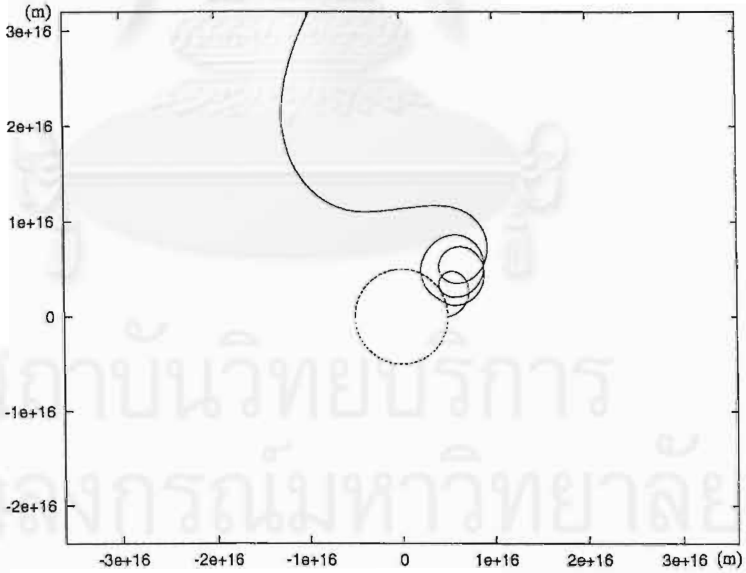

Figure 4.9: The result for momentum 4.30×10^{-12} kg m/s ($\gamma \approx 8.57 \times 10^{6}$).

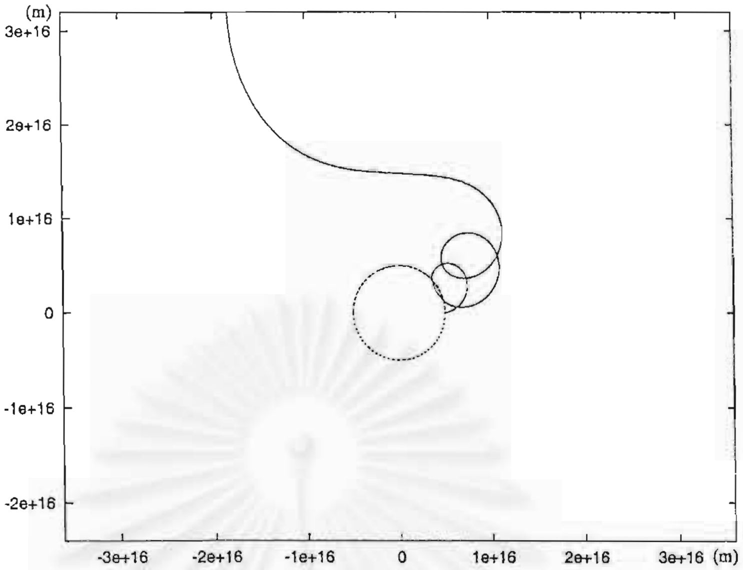

Figure 4.10: The result for momentum 4.50×10^{-12} kg m/s ($\gamma \approx 8.97 \times 10^{6}$).

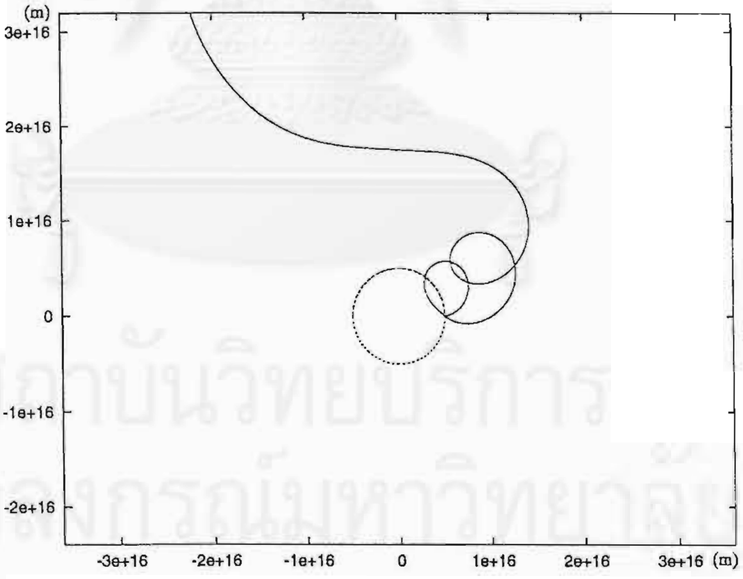

Figure 4.11: The result for momentum 4.70×10^{-12} kg m/s ($\gamma \approx 9.37 \times 10^{6}$).

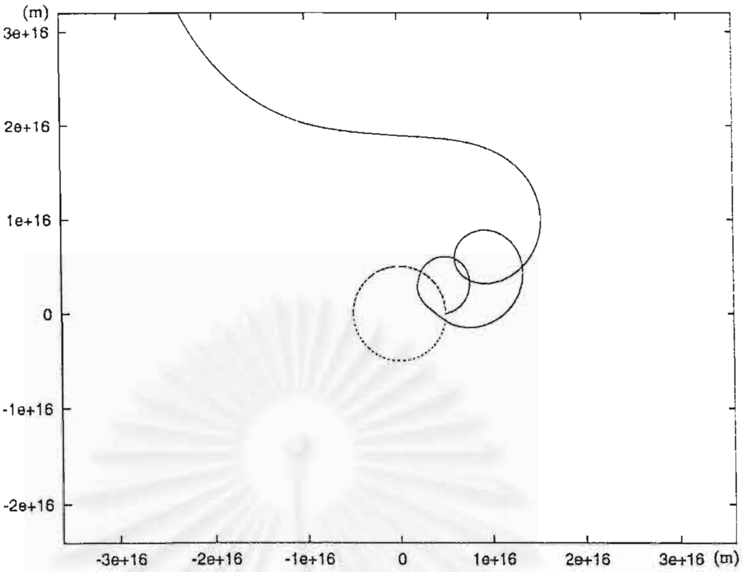

Figure 4.12: The result for momentum 4.80 × 10^{-12} kg m/s ($\gamma \approx 9.56 \times 10^6$).

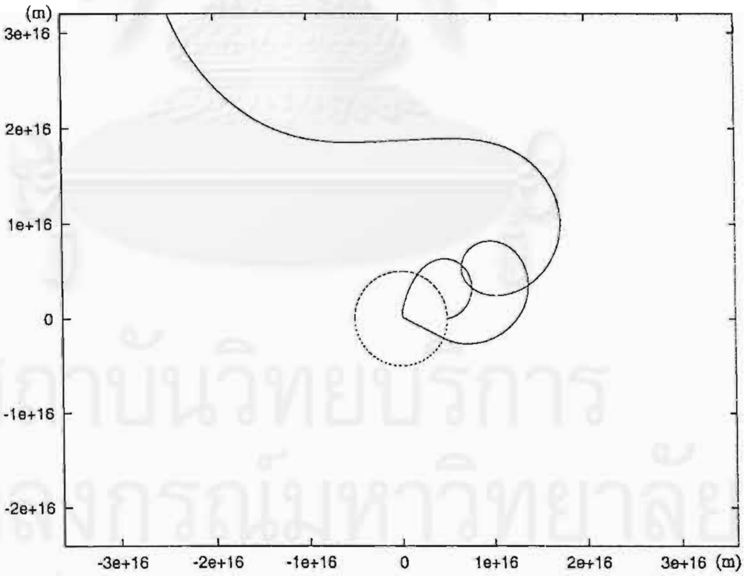

Figure 4.13: The result for momentum 4.885 × 10^{-12} kg m/s ($\gamma \approx 9.68 \times 10^6$).

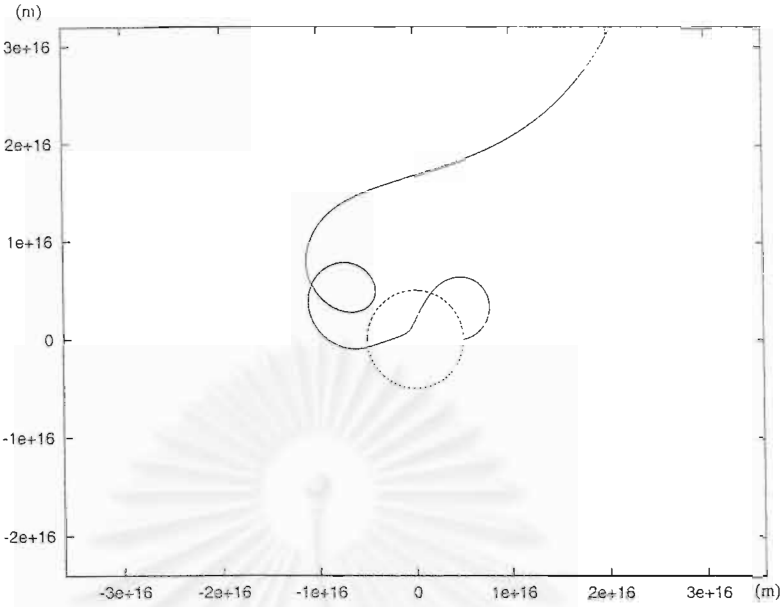

Figure 4.14: The result for momentum 4.90×10^{-12} kg m/s ($\gamma \approx 9.76 \times 10^{6}$).

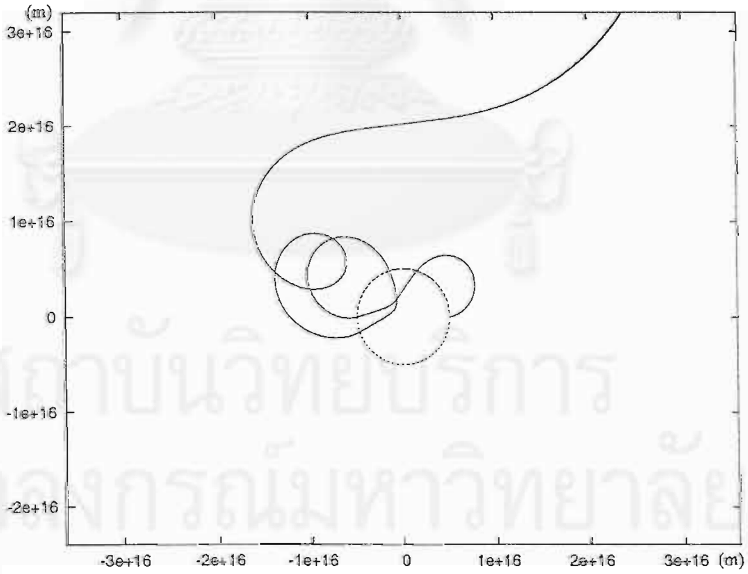

Figure 4.15: The result for momentum 4.92×10^{-12} kg m/s ($\gamma \approx 9.80 \times 10^{6}$).

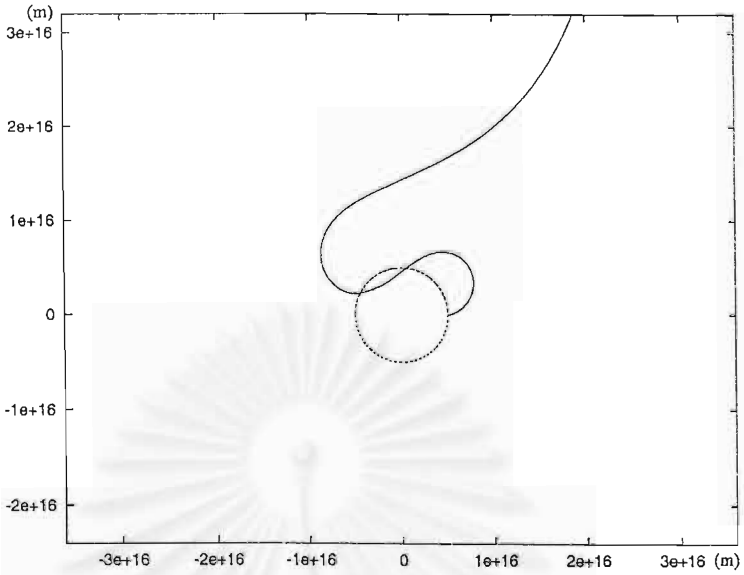

Figure 4.16: The result for momentum 5.00×10^{-12} kg m/s ($\gamma \approx 9.96 \times 10^{6}$).

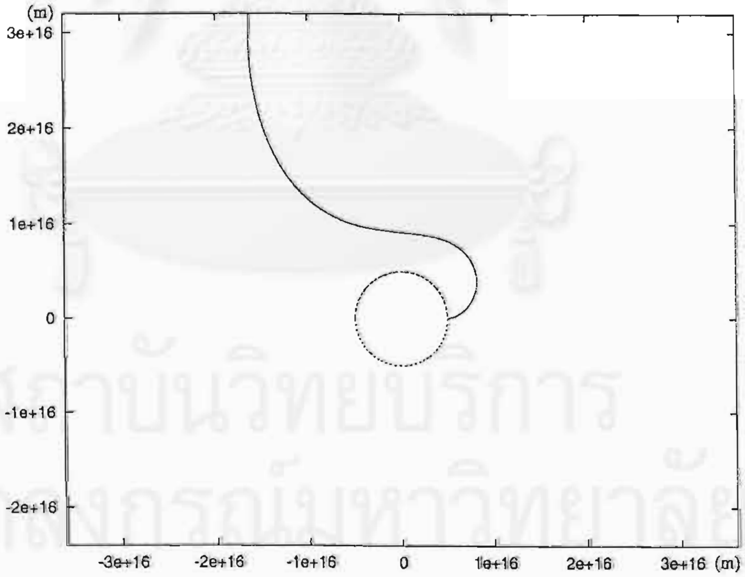

Figure 4.17: The result for momentum 5.46×10^{-12} kg m/s ($\gamma \approx 10.88 \times 10^{6}$).

as $4.3 - 4.885 \times 10^{-12}$ kg m/s, for which the particle crosses the shock. For these cases, there is shock-drift acceleration, i.e., motion along **E**, but at the same time drift outside the shock cause the particle to lose energy. The direction of **E**, in which particles gain energy, is from the north pole to the equator or the direction of polar angle increase.

We can estimate the energy change if the particle drifts from the equator to the pole (losing energy) or from the pole to the equator (gaining energy). Physically, the maximum energy change by the shock drift mechanism is the potential difference V along the termination shock from the equator to the pole, $\theta = \pi/2$ to $\theta = 0$:

$$\begin{aligned} V &= -\int \mathbf{E} \cdot d\mathbf{x} \\ &= -\int E r d\theta, \end{aligned}$$

where **E** is as in Eq. 4.7, and then

$$\begin{aligned} V &= \int_{\pi/2}^{0} \frac{cB_0 R_s \sin\theta}{R_s} R_s d\theta \\ &= -cB_0 R_s. \end{aligned} \tag{4.9}$$

The voltage difference V is of magnitude 75×10^{14} eV or 7,500 TeV. This is the approximate value of the maximum energy gain if particles drift to the equator. Our suggestion for a more complicated simulation model would be to consider more realistic situations such as a wind velocity depending on the latitude of the pulsar like in the case of the solar wind termination shock and a corresponding magnetic structure model.

However, in these simulations we did not add the effect of pitch angle scattering which in this case is an important effect. Gallant and Arons (1994) have estimated $\delta B/B \approx 0.1$, which means there is high turbulence and pitch angle scattering. If this effect plays an important role, we expect that a fraction of the particles will return to the shock and drift in the direction of energy gain. For example, in Figs. 4.11 to 4.13, if pitch angle scattering makes the particles hit the shock again at in a different angle and leads to shock drift to a lower latitude, these particles will gain energy.

Indeed, such scattering lies at the heart of standard diffusive shock acceleration (e.g., Bell, 1978). In this case, the transport equation and Rankine-Hugoniot conditions derived in Chapter 3 might be approximately valid. Both methods of analysis involve simplifying assumptions: the particle orbits shown here neglect pitch angle scattering, which our results show to be potentially important, in contrast to the work of Bell (1992) and Lucek and Bell (1994), who did not require pitch angle scattering. On the other hand, the transport equations assumes a planar geometry, which is not very accurate given the large ratio of the particle gyroradius to the shock radius. Also, such a transport equation simplifies the dynamics within a gyroradius of the shock, even when the particle orbits are taken into account in transferring particles across the shock, as in the work of Sanguansak and Ruffolo, (1999). Therefore, our results indicate that proper modeling of particle acceleration at a PWTS should incorporate both the particle trajectory calculations, as performed here, and pitch angle scattering due to random magnetic fields (Sukonthachat, 1999; Ruffolo and Sukonthachat, 1999). This would therefore be a Monte Carlo calculation (with particles perhaps starting at the thermal velocity), either by the method of Kirk and Schneider (1987), or by tracing particle orbits in turbulent magnetic fields (e.g., as in orbit calculations by Tanyong 1999 for fields calculated as in Sukonthachat, 1999; Ruffolo and Sukonthachat, 1999).

There is another mechanism that is claimed to accelerate particles to gain energies of up to 1000 times their initial energy (Bell, 1992; Lucek and Bell, 1994).

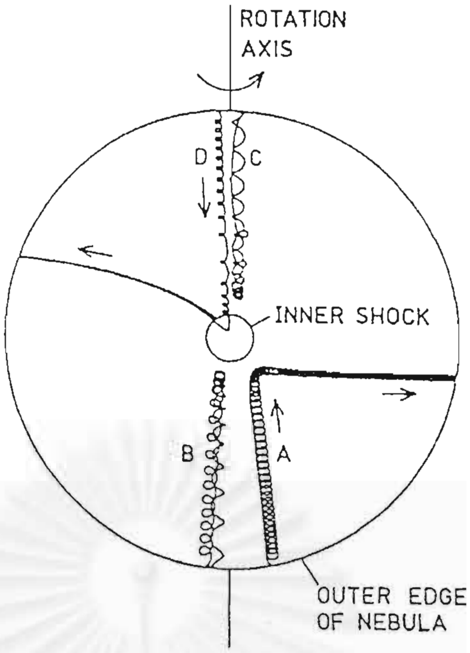

Figure 4.18: The trajectory of four cosmic rays as they pass through the nebula. In this figure only trajectory D leads to an energy gain (Lucek and Bell, 1994).

This mechanism differs from our mechanism because it accelerates particles from outside the Crab nebula as in Fig. 4.18.

On the other hand, our simulation indicates one further problem for any of these mechanisms: the strong tendency that once particles leave the shock, they drift back toward the north pole and lose energy again. This is because we have assumed $B_\phi \propto 1/r$ (as in Fig. 2.6, from Michel, 1991), and in this case the gradient drift is antiparallel to E and the drift in the outer nebula. On the other hand, Bell (1992) assumed $B_\phi \propto r$, following older work of Rees and Gunn (1974), and thus obtained a gradient drift parallel to E. In fact, the true dependence of B_ϕ on r is not known. Therefore, we conclude that whether acceleration at a SWPT really results in high-energy cosmic rays leaving the nebula depends critically on the nature of drifts outside the shock.

Chapter 5

Summary and Conclusions

After the discovery of pulsars in 1967, models of pulsars were developed continuously by many people. The interaction between the pulsar and the outer environment is of interest because we expect that in the interaction of the pulsar and the nebula there are shocks. The pulsar wind termination shocks (PWTS) are analogous to the solar wind termination shocks but PWTS are relativistic and more energetic. The pulsar that we use as the prototype of pulsars is the Crab pulsar. Goldreich and Julian (1960) concluded that a rotating magnetic neutron star cannot be surrounded by a vacuum, but rather should be surrounded by the powerful plasma ejected from the pulsar. The aligned rotation pulsar model (i.e., aligned rotation and magnetic dipole axes, Goldreich and Julian, 1969) can yield an estimate of the toroidal magnetic field, $B_t \approx 4 \times 10^{-4}$ to 4×10^{-5} Gauss at $r \approx 0.1$ to 1.0 parsecs, respectively, and a maximum energy to which charges are accelerated in the Crab pulsar as $E_{max} \approx 2 \times 10^{16} Z$ eV. More realistic models of pulsars, with oblique rotation (Ostriker and Gunn, 1969; Mestel, 1971), estimate the maximum energy as $E_{max} \approx 2 \times 10^{13}$ eV for electrons. The other component of plasma from pulsars is an electron-positron plasma from pair production at the polar cap of a pulsar (Arons, 1970, 1983 cited by Michel, 1991). After scientists found that there should be plasma around pulsars which has a very strong magnetic field, the interaction of the flow and the magnetic field became a topic of great interest.

If we accept the explanation of optical wisps by Gallant and Arons (1994), then their successful fit provides evidence for a mainly toroidal magnetic field, and even provides the rate of pitch angle scattering. In our magnetic field model used in the simulations, we use a simple form of the magnetic field as perfectly toroidal, with the magnitude of this field depending only on the polar angle.

To explore the possibility of particle acceleration at a superluminal PWTS, we have a) constructed a transport equation in Fokker-Planck form that describes diffusive shock acceleration at a relativistic shock, and b) traced orbits of particle motion in model **B** and **E** fields near a PWTS. From particle orbit simulations, most particles cross the shock only once, but there are some momentum values for which particles cross the shock again. However, for these momenta the particle drifts from the equator to the pole, which is the direction of energy loss for this case. Unlike Bell (1992) and Lucek and Bell (1994), we expect that pitch angle scattering should have an important effect in that a fraction of the particles could return to the shock making the particle drift in the direction in which the particle repeatedly gains energy. Our results show that to properly approach this problem, neither the particle orbit nor transport equation method is sufficient because each of them has limitations; pitch angle scattering is not included in the particle orbit method and the transport equation uses a planar geometry and only approximately treats dynamics within a gyroradius of the shock. Even if particles are accelerated near the shock, our particle orbit simulations show that the particles may well lose their energy due to drifts once they travel outside the shock, in which case particles outside the pulsar nebula that could be high energy cosmic rays are not produced. This result is strongly dependent on the assumed dependence of B on r, and hence represents a major uncertainty in any calculations of particle acceleration by a pulsar wind termination shock.

References

Aschenbach, B., and Brinkmann, W. "A Model of the X-ray Structure of the Crab Nebula," *Astronomy and Astrophysics* **41** (1975): 147-151.

Begelman, M. "Instability of Toroidal Magnetic Field in Jets and Plerions," *The Astrophysical Journal* **439** (1998): 291-300.

Bell, A. R. "The Acceleration of Cosmic Rays in Shock Fronts-I," *Monthly Notices of the Royal Astronomical Society* **122** (1978): 147-156.

Bell, A. R. "Cosmic Ray Acceleration in Pulsar-Driven Supernova Remnants," *Monthly Notices of the Royal Astronomical Society* **257** (1992): 493-500.

Blandford, R. D., and Ostriker, J. P. "Particle Acceleration by Astrophysical Shock," *The Astronphysical Journal* **221** (1978): L24-L32.

Coroniti, F. V. "Magnetically Striped Relativistic Magnetohydrodynamics Winds: the Crab Nebula Revisited," *The Astrophysical Journal* **349** (1990): 538-545.

de Hoffmann, F., and Teller, E. "Magneto-Hydrodynamic Shocks," *Physical Review* **80** (1950): 692-703.

Earl, J. A. "The Effect of Convection Upon Charged Particle Transport in Random Magnetic Fields," *The Astrophysical Journal* **278** (1984): 825-840.

Fermi, E.,"On the Origin of the Cosmic Radiation," *Physical Review* **75** (1949): 1169-1174.

Gallant, Y. A., and Arons, J. “Structure of Relativistic Shocks in Pulsar Winds: Model of the Wisps in the Crab Nebula,” *The Astrophysical Journal* **435** (1994): 230-260.

Goldreich, P., and Julian, W. H. “Pulsar Electrodynamics.” *The Astrophysical Journal* **157** (1969): 869-880.

Goldstein, H. *Classical Mechanics, second edition.* Reading, Massachusetts: Addison-Wesley, 1980, pp. 555-561.

Hester, J. J. et al. “WFPC2 Studies of the Crab Nebula. I. *HST* and *ROSAT* Imaging of the Synchrotron Nebula.” *The Astrophysical Journal* 448 (1995): 240-263.

Hewish, A., Bell, S. J., Pilkington, J. D. H., and Collins, R. A. “Observation of a Rapidly Pulsating Radio Source.” *Nature* **217** (1968): 709-713.

Hillas, A. M., *Annual Reviews of Astronomy and Astrophysics* **22** (1984): 425.

Jackson, J. D. *Classical Electrodynamics, second edition.* New York: John Wiley & Sons, 1975, pp. 391-400.

Kirk, J. G. “Pitch-Angle Anisotropy of Low-Energy Ions at Interplanetary Shocks,” *The Astrophysical Journal* **324** (1988): 557-565.

Kirk, J. G., and Schneider, P. “On the Acceleration of Charged Particles at Relativistic Shock Fronts,” *The Astrophysical Journal* **315** (1987): 425-433.

Lagage, P. O., and Cesarsky, C., “The Maximum Energy of Cosmic Rays Accelerated by Supernova Shock,” *Astronomy and Astrophysics* **125** (1983) :249-257.

Landau, L. D., and Lifshitz, E. M. *Fluid Mechanics.* Oxford: Pergamon Press, 1963, pp. 319-323.

Lipunov, V. M. *Astrophysics of Neutron Stars.* New York: Springer-Verlag, 1992, pp. 6-9.

Longair, M. S. *High Energy Astrophysics Vol.1-2, second edition.* Cambridge: Cambridge University Press, 1997, pp. 271-272.

Lucek, S. G., and Bell, A. R. "Cosmic Ray Acceleration in Inhomogeneous Magnetic Field about Relativistic Shocks." *Monthly Notices of the Royal Astronomical Society* **268** (1994): 581-594.

Mestel, L. "Pulsar Magnetospheres." *Nature Physical Science* **233** (1971): 149-152.

Michel, F. C. *Theory of Neutron Star Magnetospheres.* Chicago: The University of Chicago Press, 1991, pp. 103-108.

Ostlie, D. A., and Carroll, B. W. *An Introduction to Modern Stellar Astrophysics.* Reading, Massachusetts: Addison-Wesley, 1996, pp. 598-603.

Ostriker, J. P., and Gunn, J. E. "On the Nature of Pulsars. I. Theory," *The Astrophysical Journal* **157** (1969): 1395-1417.

Press, W. H., Flannery, B. P., Teukolsky, S. A., and Vetterling, W. T. *Numerical Recipes In C.* New York: Cambridge University Press, 1988, pp. 574-579.

Protheroe, R. J. "Origin and Propagation of the Highest Energy Cosmic Rays," in *Towards the Millennium in Astrophysics: Problems and Prospects*, eds. Shapiro, M. M., and Wefel, J. P. Singapore: World Scientific, 1996, pp. 1-27.

Rees, M. J., and Gunn, J.E. "The Origin of the Magnetic Field and Relativistic Particles in the Crab Nebula," *Monthly Notices of the Royal Astronomical Society* **167** (1974): 1-12.

Ruffolo, D. "Effect of Adiabatic Deceleration on the Focused Transport of Solar Cosmic Rays," *The Astrophysical Journal* **442** (1995): 861-874.

Ruffolo, D. "Transport and Acceleration of Energetic Charged Particles near an Oblique Shock," *The Astrophysical Journal* **515** (1999): 787-800.

Ruffolo, D., and Chuychai, P. "First-Order Fermi Acceleration at a Continuous Compression," *26th International Cosmic Ray Conference* **6** (1999): 552-555.

Ruffolo, D., and Sukonthachat, J. "Multiple Magnetic Field-Shock Crossing and Particle Acceleration at Quasi-perpendicular Shocks," *26th International Cosmic Ray Conference* **7** (1999): 476-479.

Sanguansak, N., and Ruffolo, D. "A Hybrid Orbit-Finite Difference Treatment of Oblique Shock Acceleration," *26th International Cosmic Ray Conference* **4** (1999): 459.

Shklovskii, I. S. "On the Origin of Cosmic Rays," *Dokl. Akad. Nauk SSSR* **91** (1953): 475-478.

Sukonthachat, J. *Multiple Magnetic Field-Shock Crossings and Particle Acceleration at Quasi-Perpendicular Shocks.* M.Sc. Thesis, Department of Physics, Graduate School, Chulalongkorn University, 1999.

Tanyong, N. *Simulation of Diffusion of Cosmic Ray Particles.* Senior Project, Department of Physics, Faculty of Science, Chulalongkorn University, 1998.

Terasawa, T., "Acceleration of Cosmic Rays (I), (II)." in *JSPS-ICRR International Spring School '95 Cosmic Rays in Contemporary Astrophysics*, eds. Yuda, T., and Hayashida, N. Tokyo: Institute for Cosmic Ray Research, University of Tokyo, 1995, p. 172.

van den Bergh, S., and Pritchet, C. J. "The Crab Synchrotron Nebula at $0''.5$ Resolution," *The Astrophysical Journal* **338** (1989): L69-L70.

Appendix A

Program Usage

Most of following is adapted from programs in Press et al. (1988).

```
#include"stdio.h"
#include"math.h"
#include"stdlib.h"

#define  PGROW     -0.2
#define  PSHRNK    -0.25
#define  FCOR       0.06666666
#define  SAFETY     0.9
#define  ERRCON     6.0e-4
#define  SMALL      1.0e-6
#define  MAXSTP     20000
#define  TINY       1.0e-30
#define  q     -1.6021e-19 /*coulomb*/
#define  c     3.0e8 /*m/s*/
#define  Rs         5.0e15 /*m*/

int kmax=0, kount=0;
double *xp=0, **yp=0,dxsav=0;


void odeint(ystart,nvar,x1,x2,eps,h1,hmin,nok,nbad,derivs,rkqc)
double ystart[],x1,x2,eps,h1,hmin;
int nvar,*nok,*nbad;
void (*derivs)();
void (*rkqc)();
{
   double xsav,x,hnext,hdid,h;
   double *yscal,*y,*dydx,*dvector();
   int nstp,i;
   void nrerror(),free_dvector();
   FILE *fpt1,*fpt2,*fpt3,*fpt4,*fpt5,*fpt6;

   fpt1  = fopen("x.dat","w");
   fpt2  = fopen("y.dat","w");
   fpt3  = fopen("z.dat","w");
   fpt4  = fopen("px.dat","w");
   fpt5  = fopen("data1.dat","w");
   fpt6  = fopen("data2.dat","w");

   yscal = dvector(1,nvar);
   y     = dvector(1,nvar);
   dydx  = dvector(1,nvar);
   x     = x1;
   h     = (x2>x1)? fabs(h1):-fabs(h1);
   *nok  = (*nbad) = kount = 0;
   for (i=1;i<=nvar;i++) y[i]=ystart[i];
   if(kmax>0) xsav=x-dxsav*2.0;
   for(nstp=1;nstp<=MAXSTP;nstp++){
      (*derivs)(x,y,dydx);
      for(i=1;i<=nvar;i++)
         yscal[i]=fabs(y[i])+fabs(dydx[i]*h)+TINY;
```

```
     if(kmax>0){
if(fabs(x-xsav)>fabs(dxsav)){
   if(kount<kmax-1){
     xp[++kount]=x;
     for(i=1;i<=nvar;i++) yp[i][kount]=y[i];
     xsav=x;
   }
}
     }
     if((x+h-x2)*(x+h-x1)>0.0) h=x2-x;
     (*rkqc)(y,dydx,nvar,&x,h,eps,yscal,&hdid,&hnext,derivs);
     fprintf(fpt1,"%le\n",y[1]);
     fprintf(fpt2,"%le\n",y[2]);
     fprintf(fpt3,"%le\n",y[3]);
     fprintf(fpt4,"%le\n",y[4]);
     fprintf(fpt5,"%le       %le       %le\n",sqrt(y[4]*y[4]+y[5]*y[5]+y[6]*y[6]),
             sqrt(y[1]*y[1]+y[2]*y[2]+y[3]*y[3]),y[1]);
     fprintf(fpt6,"%25.4lf %25.4lf %25.4lf\n",y[1],y[2],y[3]);
     if(hdid==h) ++(*nok); else ++(*nbad);
     if((x-x2)*(x2-x1)>=0.0){
        for(i=1;i<=nvar;i++) {
           ystart[i]=y[i];
        }
if(kmax){
   xp[++kount]=x;
   for (i=1;i<=nvar;i++) yp[i][kount]=y[i];
        }
        free_dvector(dydx,1);
        free_dvector(y,1);
        free_dvector(yscal,1);
        return;
     }
     if (fabs(hnext)<=hmin) nrerror("Step size too small in ODEINT");
     h=hnext;
   }
   nrerror("Too many steps is routine ODEINT");
   fclose(fpt1);
   fclose(fpt2);
   fclose(fpt3);
   fclose(fpt4);
   fclose(fpt5);
   fclose(fpt6);
}


void *derivs(x,y,dydx)
double x, y[], dydx[];
{
   double Bx(), By(), Bz(), Ux(), Uy(), Uz();
   int i;

   dydx[1] = y[4]/sqrt(y[4]*y[4]+y[5]*y[5]+y[6]*y[6])*c;
   dydx[2] = y[5]/sqrt(y[4]*y[4]+y[5]*y[5]+y[6]*y[6])*c;
   dydx[3] = y[6]/sqrt(y[4]*y[4]+y[5]*y[5]+y[6]*y[6])*c;
   dydx[4] = q*((-dydx[3])*By(y[1],y[2],y[3])+Uz(y[1],y[2],y[3])*
             By(y[1],y[2],y[3]));
   dydx[5] = q*((dydx[3])*Bx(y[1],y[2],y[3])-Uz(y[1],y[2],y[3])*
             Bx(y[1],y[2],y[3]));
   dydx[6] = q*((dydx[1]*By(y[1],y[2],y[3])-dydx[2]*Bx(y[1],y[2],y[3]))
             -(Ux(y[1],y[2],y[3])*By(y[1],y[2],y[3])-Uy(y[1],y[2],y[3])
             *Bx(y[1],y[2],y[3])));
}

double Ux(x,y,z)
double x,y,z;
```

```
{
   double r;
   r=sqrt(x*x+y*y+z*z);
   if(r<Rs) return c*x/r;
    else return (c/3)*x/r;
}

double Uy(x,y,z)
double x,y,z;
{
   double r;
   r=sqrt(x*x+y*y+z*z);
   if(r<Rs) return c*(y/r);
   else return (c/3)*(y/r);
}

double Uz(x,y,z)
double x,y,z;
{
   double r;
   r=sqrt(x*x+y*y+z*z);
   if(r<Rs) return c*(z/r);
   else return (c/3)*(z/r);
}


double Bx(x,y,z)
double x, y, z;
{
   double r,bx;

   r=sqrt(x*x+y*y+z*z);
   if(r<Rs)
      bx = -5.0e-9/*Rs*y*sqrt(x*x+y*y)/(r*r*r)*/;
   else
      bx = -3.0*5.0e-9/*Rs*y*sqrt(x*x+y*y)/(r*r*r)*/;
   return bx;
}


double By(x,y,z)
double x,y,z;
{
   double r,by;

   r=sqrt(x*x+y*y+z*z);
   if(r<Rs)
      by = 5.0e-9/*Rs*x*sqrt(x*x+y*y)/(r*r*r)*/;
   else
      by = 3.0*5.0e-9/**Rs*x*sqrt(x*x+y*y)/(r*r*r)*/;
/**/printf("By is %le \n",by);
  return  by;
}


void rkqc(y, dydx, n, x ,htry, eps, yscal, hdid, hnext, derivs)
double y[], dydx[], *x, htry, eps, yscal[], *hdid, *hnext;
void (*derivs)(); /* ANSI: void (*derivs)(float,float*,float *); */
int  n;
```

/* Fifth-order Runge-Kutta step with monitoring of local truncation error to ensure accuracy and adjust stepsize. Input are the dependent variable vector y[1..n] and its derivative dydx[1..n] at the starting value of the dependent variables x. Also input are the stepsize to be attemped htry, the required accuracy eps. and the vector ysca[1..n] against which the error is scaled. On output,y and x are replaced by their new values.hdid is the stepsize which was actually accomplished , and hnext is the estimated next stepsize. derivs is the user-supplied routine that computes the right-hand side derivatives(output are dydx[1..n])*/

```
{
  int i;
  double xsav, hh, h, temp, errmax;
  double *dysav,*ysav,*ytemp,*dvector();
  void rk4(),nrerror(),free_dvector();

  dysav = dvector(1,n);
  ysav  = dvector(1,n);
  ytemp = dvector(1,n);
  xsav  = (*x); /* Save initial values. */
  for(i=1;i<=n;i++) {
     ysav[i]  = y[i];
     dysav[i] = dydx[i];
  }
  h=htry; /* Set stepsize to the initial trial value.*/
  for(;;) {
     hh = 0.5*h; /* Take two half steps. */
     rk4(ysav, dysav, n, xsav, hh, ytemp,derivs);
     *x = xsav+hh;
     (*derivs)(*x, ytemp, dydx);
     rk4(ytemp, dydx, n, *x, hh, y, derivs);
     *x = xsav+h;
     if(*x==xsav) nrerror("Stop size too small in routine RKQC");
     rk4(ysav,dysav,n,xsav,h,ytemp,derivs); /*Take the large step.*/
     errmax=0.0;
     for(i=1;i<=n;i++) {
       ytemp[i]=y[i]-ytemp[i]; /* ytemp now contains the error estimate.*/
        temp=fabs(ytemp[i]/yscal[i]);
        if(errmax < temp) errmax = temp;
     }
     errmax /=eps; /* Scale relative to required tolerance.*/
     if(errmax<=1.0) { /* Step succeeded. Compute size of next step. */
       *hdid=h;
 *hnext=(errmax> ERRCON ?
     SAFETY*h*exp(PGROW*log(errmax)) : 4.0*h);
 break;
     }
     h = SAFETY*h*exp(PSHRNK*log(errmax));/*Turncation error too large, reduce step size*/
   }
   for(i=1;i<=n;i++) {
      y[i]+=ytemp[i]*FCOR; /* Mop up fifth-order truncation error.*/
   }
   free_dvector(ytemp,1);
   free_dvector(dysav,1);
   free_dvector(ysav,1);
}

void rk4(y, dydx, n, x, h, yout,derivs)
double y[], dydx[], x, h, yout[];
void (*derivs)(); /* ANSI: void (*derivs)(float,float *,float *);*/
int n;
```

/* Given value for n variables y[1..n] and their derivatives dydx[1..n] known at x, use the fourth-order Runge-Kutta method to advance the solution over an interval h and return the incremented variables ar yout[1..n],which need not be a distinct array from y.The user supplies the routine derivs(x, y, dydx) which return derivatives dydx at x. */

```
{
   int i;
   double xh, hh, h6, *dym, *dyt, *yt,*dvector();
   void free_dvector();

   dym=dvector(1,n);
   dyt=dvector(1,n);
   yt=dvector(1,n);
   hh=h*0.5;
   h6=h/6.0;
   xh=x+hh;
   for(i=1;i<=n;i++) yt[i]=y[i]+hh*dydx[i]; /* First step */
   (*derivs)(xh ,yt, dyt);                  /* Second step */
   for(i=1;i<=n;i++) yt[i]=y[i]+hh*dyt[i];
   (*derivs)(xh, yt, dym);                  /* Third step */
   for(i=1;i<=n;i++) {
      yt[i]=y[i]+h*dym[i];
      dym[i]+=dyt[i];
   }
   (*derivs)(x+h, yt, dyt);                  /* Fourth step */
   for(i=1;i<=n;i++) /* Accumulate increments with proper weights.*/
     yout[i]=y[i]+h6*(dydx[i]+dyt[i]+2.0*dym[i]);
   free_dvector(yt,1);
   free_dvector(dyt,1);
   free_dvector(dym, 1);
}

void main(void)
{
   int nvar,i;
   double ystart[7],x1,x2,eps,h1,p;
   double hmin,nok,nbad;
   void (*derives)();
/*   FILE *shock;

   shock = fopen("s.dat","w");*/
   ystart[1] = Rs-5.0e13/*cos(0.1745)*/;
   ystart[2] = 0.0;
   ystart[3] = 0.0/*Rs*sin(0.1745)*/;
   ystart[4] = 3.22e-12*cos(0.1745)/1863.0; /*  initial momentum*/
   ystart[5] = 0.0;
   ystart[6] = 3.22e-12*sin(0.1745)/1863.0;
   nvar      = 6;
   x1        = 0.0;
   x2        = 8.0e7;
   eps       = 1.0e-6;
   h1        = 1.0e-3;
   hmin     = 0.0;
   nok      = 0.0;
   nbad     = 0.0;
   odeint(ystart,nvar,x1,x2,eps,h1,hmin,&nok,&nbad,derivs,rkqc);
/*   for(i=0;p<Rs;i++)
    {
       p=-Rs+i*1.0e10;
       fprintf(shock,"%le     %le       %le\n",p,sqrt(Rs*Rs-p*p),-sqrt(Rs*Rs-p*p));
    }
    fclose(shock);

}*/
```

Curriculum Vitae

Anant Eungwanichayapant.

1974 Born: May, 9th 1974 in Khon Kaen, THAILAND.
Father: Pon Eungwanichayapant.
Mother: Upsorn Sae-Hear.

1992-1996 Bachelor of Science (Physics),
Chulalongorn University, Bangkok, THAILAND.

หอสมุดกลาง สถาบันวิทยบริการ จุฬาลงกรณ์มหาวิทยาลัย